Steffen Emil Snippen Moe

Simulation and Fabrication of Mach-Zehnder Interferometer-Assisted Ring Resonator Configuration (MARC) Photonic Sensors

TFE4570 - Nanoelectronics and Photonics, Specialization Course
Supervisor: Astrid Aksnes
Co-supervisor: Jens Høvik
Trondheim, July 2023

Norwegian University for Science and Technology
Department of Electronic Systems

NTNU
Norwegian University of
Science and Technology

Abstract

Photonic devices based on Silicon-on-insulator (SOI) technology has been studied extensively the past years due to their use in photonic integrated circuits (PIC). This technology can be utilized in the field of biosensing to detect different concentrations of viruses, bacteria, and other biological material, e.g. insulin. a Mach-Zehnder interferometer assisted ring resonator configuration (MARC) sensor can be able to detect several biological compounds through its ability to multiplex several individual signals. The ability to multiplex the signals comes from the angular separation in the add-drop ring resonators, where different separation angles are used to obtain different transmission spectra.

In this project, a finite-elements based (FEM) COMSOL Multiphysics 6.0 has be used to investigate the aforementioned MARC device. By simulating three different MARC sensors with an angular separation of 90° (MARC90), 135° (MARC135), and 240° (MARC240), it has been possible to simulate sensors that can be fabricated in a lab in the future.

The three different MARC sensors shows promising results with a quality factor of 6400, 7800, and 2500 for the MARC240, MARC90, and MARC135, respectively. However, the MARC135 does show imbalances. A multiplexed MARC sensor was also simulated, but the signal was affected by the aforementioned imbalance. The simulated sensors were also fabricated at NTNU NanoLab.

The transmission spectrum from the fabricated MARC sensors were characterized using a tunable laser, which coupled into the MARC sensors. Only the MARC240 sensors yielded a high-quiality signal, while the MARC90, MARC135 and multiplexed MARC were influenced by too much noise and bad coupling.

Preface

This project completes my degree at NTNU in Nanotechnology (MTNANO) at NTNU. This work is the continuation of my project last autumn [1]. Chapter 1 and Chapter 2 is based heavily upon the aforementioned project, while Chapter 3 has been modified but is still similar to Chapter 3 in [1]. Most chapters have been expanded upon and parts are rewritten.

Most concepts are based upon the work of Yadav et al. [2, 3]. However, the fabrication process has been a lot of trail and error, and has taken most of the time during this project. The measurements did not turn out as expected, and made it difficult to assess what went wrong. It has been a steep learning curve during this project, and I am happy to have finished.

Steffen Moe

Steffen Emil Snippen Moe
Trondheim, July 10th 2023

Acknowledgements

First of all my supervisor Astrid Aksnes deserves my gratitude for the help and support she has been giving me during this project. she has been enthusiastic and helpful with my work throughout the semester, something that has helped with my motivation. Also my co-supervisor Jens Høvik has been helping out a lot when it comes to how COMSOL works and how to do the fabrication process. I would also give my sincerest gratitude to Mukesh Yadav, who took time out of this days to mentor me on the MARC device. Thank you for all the hours you spent on making me understand the device you once worked on. Lastely I want to thank my fellow students, Joakim Ekern and Peter Nikolai Kaasa Sundgaard for sitting next to me during this semester and helping me out.

Contents

Abstract **i**

Acknowledgements **iii**

Contents **v**

1 Introduction **1**

2 Theory **3**
2.1 Electromagnetic Theory of Light 3
2.2 Interference 6
2.2.1 Interferometry 7
2.3 Waveguides 8
2.3.1 Planer Mirror Waveguide 8
2.3.2 Planar Dielectric Waveguide 10
2.3.3 Rectangular Dielectric Waveguide 11
2.3.4 Evanescence and Coupling between Waveguides 11
2.4 Optical Resonators 12
2.4.1 Fabry-Perot Resonator 12
2.4.2 Ring Resonator 14
2.5 MARC Device 17
2.5.1 Spectral Line Shapes 19
2.5.2 Multiplexed MARC Device 20
2.5.3 MARC Device as Sensor 20

3 Methods **21**
3.1 Theoretical framework 21
3.2 COMSOL Simulations 22
3.2.1 Effective Mode Index Analysis 25
3.3 Fabrication 26
3.3.1 Silicon-on-Insulator 27
3.3.2 Plasma-Enhanced Chemical Vapor Deposition 27

3.3.3 Electron Beam Lithography 29
3.3.4 Inductively Coupled Plasma-Reactive Ion Etching 32
3.3.5 Photolitography 34
3.4 Characterization Tools 34
3.4.1 Optical Microscope 34
3.4.2 Scanning Electron Microscopy 35
3.4.3 Interaction Volume 35

4 Experimental Procedure 38
4.1 COMSOL simulations 38
4.1.1 Physical Setup 39
4.1.2 Parameters 39
4.1.3 Preliminary Simulations 40
4.1.4 3dB Coupler 41
4.1.5 Ring Resonators 41
4.1.6 Mach-Zehnder Interferometer 41
4.1.7 MARC Sensors 42
4.2 Fabrication and Characterization 43
4.2.1 Thin Film 43
4.2.2 Mask Pattern 45
4.2.3 Etch 47
4.2.4 Inverted Tapers 47
4.2.5 Scribing and Breaking 48
4.2.6 SEM 49
4.3 Transmission Spectrum Setup 49

5 Results and Discussion 50
5.1 Individual Components 50
5.1.1 3dB Coupler 50
5.1.2 Ring Resonators 52
5.1.3 Mach-Zehnder Interferometer 54
5.2 MARC Simulations 55
5.2.1 MARC240 55
5.2.2 MARC90 57
5.2.3 MARC135 58
5.2.4 Multiplexed MARC 59
5.2.5 Fabrication Results 60
5.2.6 MARC Measurements 62
5.2.7 MARC240 62
5.2.8 MARC90 64
5.2.9 MARC135 66
5.3 Multiplexed MARC 67

6 Conclusion **68**
6.0.1 Simulations 68
6.0.2 Fabrication 68

7 Further Work **69**

References **71**

1 | Introduction

The field of medicine is constantly improving, which has led to an increase in the life expectancy, where medicinal technology is the main reason[4]. The ability to use biosensing to detect various substances such as viruses, bacteria and toxins is essential to prevent sickness[5]. Especially during the on-going pandemic, it is important to be able to detect different biological substances early to avoid an unnecessary spread[6]. This means that there is a demand for a quick and cheap way to detect biomarkers, which can improve the overall health of the world's population.

Silicon-on-insulator (SOI) based photonic sensors shows promising results, as they are inexpensive to produce and quite reliable[7]. Such biosensors operates by detecting the change in a physical, measurable quantity, e.g. intensity. By detecting the response, it is possible to determine the presence of a biological analyte[8].

The silicon is transparent in the telecommunication wavelength band (1200-1700 nm)[9]. The SOI technology can also be combined with photonic integrated circuits (PICs)[10], which can be the main components that comprises a lab-on-chip (LOC) device. These devices can measure the concentration of various biological substances[11].

A Mach-Zehnder interferometer-assisted ring resonator configuration (MARC) sensor is an interferometer that is combined with an add-drop ring resonator, which creates a unique transmission spectrum based on the geometry of the ring resonator[2]. The MARC sensor is able to have a greater measurment interval compared to a standard ring resonator, but the main benefit of such a device is the ability to multiplex several add-drop ring resonators[3]. This enables the multiplexed MARC sensor to measure several biological substances simultaneously, making it a suitable candidate for the increasing LOC application demand.

This project, as part of the same research group as Yadav et al., continues to investigate the multiplexed MARC sensor to develop a LOC application for biosensing. Three different MARC sensors are created and simulated in the finite-elements (FEM) based COMSOL Multiphysics 6.0 (COMSOL) program. By investigating the simulated transmission spectrum of the three MARC sensors, the sensors was eventually created at NTNU NanoLab and characterized in Astrid Aksnes' laser

lab.

Different measurements are carried out on the transmission spectrum from the MARC sensors and are investigated in this project. The theory behind electromagnetic waves, interferometers, waveguides, resonators, and the MARC sensor is introduced in Chapter 2. Then the simulation/fabrication methods and techniques used are explained in Chapter 3. The experimental procedure is then reviewed in Chapter 4, where a systematic step-by-step approach is used towards creating and simulating the three MARC sensors. Further more in chapter 5 the results are showcased and discussed. The results and discussion are then used to conclude in Chapter 6, where the results are used to determine which part of the process that worked and which part that did not work. Finally the future of this project is briefly explained in Chapter 7.

2 | Theory

Throughout this chapter, the relevant theoretical background needed to understand and discuss the simulations and results of this thesis will be presented. To start with, the theory behind simple electromagnetic waves will be described. Such topics includes waveguides (see Section 2.3) and resonating devices (see Section 2.4), which are important components constituting the multiplexed MARC device.

2.1 Electromagnetic Theory of Light

A brief introduction of the general theory of light will be discussed before proceeding with the advanced theory of this project. As most of this project concerns the propagation of light through waveguide devices, the discussion will start by introducing the equations of light traveling through a linear, non-dispersive, homogeneous, isotropic, and source-free medium.

Maxwell's equations in a source-free medium without surface charges are given as[12]

$$\nabla \times \mathbf{E} = -\frac{\partial \mathbf{B}}{\partial t} \tag{2.1}$$

$$\nabla \times \mathbf{H} = \frac{\partial \mathbf{D}}{\partial t} \tag{2.2}$$

$$\nabla \cdot \mathbf{D} = 0 \tag{2.3}$$

$$\nabla \cdot \mathbf{B} = 0, \tag{2.4}$$

where $\mathbf{E} = \mathbf{E}(\mathbf{r}, \mathrm{t})$ and $\mathbf{H} = \mathbf{H}(\mathbf{r}, \mathrm{t})$ is the electric field and the magnetic field, respectively. When no external field is applied, the *electric flux density* and *magnetic flux density* can be written as $\mathbf{D} = \epsilon\mathbf{E}$ and $\mathbf{B} = \mu\mathbf{H}$, respectively. $\epsilon = \epsilon_r\epsilon_0$ is the electric permittivity and $\mu = \mu_r\mu_0$ is the magnetic permeability, where the material expressions are described by the ratio of the relative value (denoted with subscript *r*) to the vacuum value (denoted with subscript *0*).

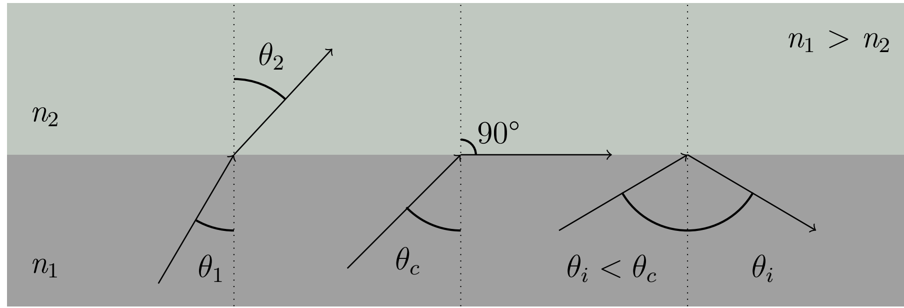

Figure 2.1: An electromagnetic wave incident on a boundary between two different media with different angles, illustrating how Snell's law, critical angle, and TIR works.

The two aforementioned material properties ϵ and μ are used to define the speed of an electromagnetic wave in a material, given by the equation[12]

$$c = \frac{1}{\sqrt{\epsilon\mu}}. \tag{2.5}$$

The constant c denotes the speed at which light travels in a dielectric medium. It is useful to look at the ratio between the speed of light in vacuum and the speed of light in a medium, which describes how the speed of light changes as it crosses the boundary between free space and the medium. This ratio is termed the *refractive index* of the medium and is given as

$$n = \frac{c_0}{c}, \tag{2.6}$$

where c_0 is the speed of light in free space. When there is a planar boundary between two different materials with refractive indices n_1 and n_2, where $n_1 > n_2$, an incident electromagnetic wave will refract when propagating through the boundary. For an electromagnetic wave incident on the boundary at an angle θ_1 from medium 1 with refractive index n_1, the refraction of the wave after crossing the boundary is described by *Snell's law*, given by

$$n_1 \sin\theta_1 = n_2 \sin\theta_2, \tag{2.7}$$

where θ_2 is the angle of the outgoing wave from the boundary. When θ_1 reaches the so-called *critical angle*, which occurs when θ_2 reaches 90°, there will be no refraction when the light reaches the boundary. The critical angle is

$$\theta_c = \sin^{-1}\frac{n_2}{n_1}. \tag{2.8}$$

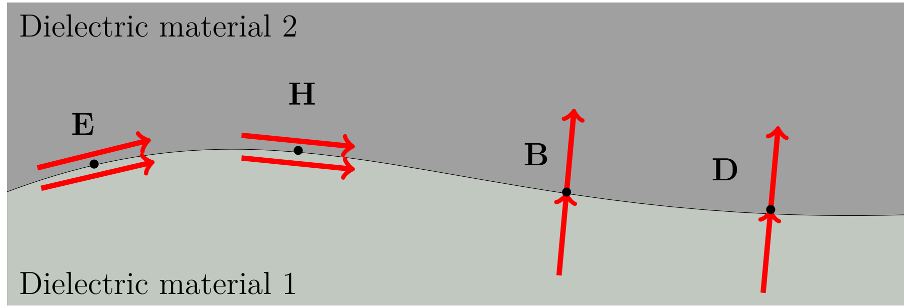

Figure 2.2: Boundary conditions for the **E**-, **H**, **B**-, and **D**-fields at the interface between dielectric materials. No surface currents or surface charges.

This relationship between n_2 and n_1 gives rise to the phenomenon of *total internal reflection* (TIR) in which light is reflected at the boundary, and thus can be confined within an area. It is more common to use the complementary angle, $\overline{\theta}_c = \pi/2 - \theta_c$, when discussing TIR. Snell's law, the critical angle, and TIR are illustrated in Figure 2.1.

By returning to Maxwell's equations, it is possible to solve them given the use of correct boundary conditions. To solve Equations 2.1-2.4, we use the boundary conditions[13]

$$E_{1t} = E_{2t} \tag{2.9}$$

$$H_{1t} = H_{2t} \tag{2.10}$$

$$D_{1n} = D_{2n} \tag{2.11}$$

$$B_{1n} = B_{2n}, \tag{2.12}$$

where it is assumed that there are no surface currents or surface charges. The subscripts t and n denote the tangential and normal components of the **E** / **H**-field and the **D** / **B**-field, respectively.

All components of the fields are required to be continuous functions of position, meaning that at the boundary the fields are identical coming from both sides of the boundary. The components of **E** and **H** need to satisfy the *wave equation*, given as[12]

$$\nabla^2 u - \frac{1}{c^2}\frac{\partial^2 u}{\partial t^2} = 0, \tag{2.13}$$

where u is the real part of the wave function. The complex wave function is given as

$$U(\mathbf{r},t) = a(\mathbf{r})e^{j\phi(\mathbf{r})}e^{j2\pi\nu t}, \tag{2.14}$$

where ν is the wave frequency and j is the imaginary number. Since u is the real part of U, u can be written as

$$u(\mathbf{r},t) = \mathrm{Re}\{U(\mathbf{r},t)\} = \mathrm{Re}\{U(\mathbf{r})e^{j\omega t}\}, \tag{2.15}$$

where $\omega = 2\pi\nu$ is the angular frequency. Inserting Equation 2.15 into Equation 2.13 yields the *Helmholtz equation* and is expressed as

$$\nabla^2 U(\mathbf{r}) + k^2 U(\mathbf{r}) = 0. \tag{2.16}$$

The constant k is derived from the angular frequency, $k = \omega\sqrt{\epsilon\mu}$, which is why it is referred to as the angular wavenumber - or more commonly as the *wavenumber*. Throughout the theory part the wavenumber will play an important role for the waveguide theory in Section 2.3.

2.2 Interference

The *intensity* I of a wave U is a measurable parameter, where it is defined as the time average unit of power per unit area that is transmitted through a area perpendicular to the propagation of the wave[14]. The energy related to a complex wave function U is given by

$$I = |U|^2. \tag{2.17}$$

If there is a superposition of N monochromatic waves, i.e. N waves consisting of one single frequency ν, the total wave function will be the sum of the individual wave functions[12, 14], given as

$$U(\mathbf{r}) = U_1(\mathbf{r}) + U_2(\mathbf{r}) + ... + U_{N-1}(\mathbf{r}) + U_N(\mathbf{r}), \tag{2.18}$$

where each term represents each of the N wave functions.

A wave that is comprised of two individual monochromatic waves, described by the two wave functions $U_1(\mathbf{r})$ and $U_2(\mathbf{r})$, will have an intensity described by the *interference equation*[12], given by

$$I = |U_1 + U_2|^2 = I_1 + I_2 + 2\sqrt{I_1 I_2}\cos\varphi, \quad \varphi = \varphi_2 - \varphi_1. \tag{2.19}$$

From Equation 2.19 it becomes clear that the intensity from the total wave is not equal to the sum of the intensities of the individual waves. This is due to the third term, which contains a factor $\sqrt{I_1 I_2}$ that is dependent on the phase between the aforementioned waves.

Given a superposition between two waves of the same intensity, i.e. $I_1 = I_2 = I_0$, it can be shown that the superposed intensity is given by

$$I = I_1 + I_2 + 2\sqrt{I_1 I_2}\cos n = \begin{cases} 4I_0 & \text{for } n = 0, 2\pi, 4\pi, ... \\ 0 & \text{for } n = \pi, 3\pi, 5\pi, ... \end{cases} . \tag{2.20}$$

This means that the phase difference φ is directly correlated to the intensity of the combined waves, and is determined solely by the phase-dependent term. The principle of a phase-dependent intensity of two waves is the concept behind interferometry.

The phase-term is very important during the simulations that are experimentally explained in Section **??**. This is because information can be extracted from a signal based on the interference of the superimposed waves.

2.2.1 Interferometry

Interferometry is a technique that gathers information from a superimposed wave - the device is called an *interferometer*[12]. The device splits an incoming wave into two outgoing waves using a beamsplitter. This creates a difference in the phase of the waves before recombining them into one single wave again. The intensity of the now superposed wave can be detected at the output, which in turn will be read as the phase difference induced in one of the waves.

Mach-Zehnder Interferometer

In a Mach-Zehnder interferometer, incoming light is divided into two equal waves in the two arms, as illustrated in Figure 5.6. An external factor, e.g. electric field, magnetic field, refractive index change, path length difference between interferometer arms, will have different optical path lengths which will result in a delayed wave during recombination. The phase delay results in an interference at the output of the Mach-Zehnder interferometer. This results in a change of intensity with a periodicity of 2π at the output spectrum. This interferometer will be utilized as the base of the simulations in the project.

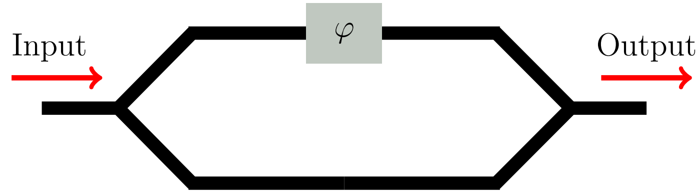

Figure 2.3: An illustrative figure of how the MZI is designed. One of the interferometer arms undergoes an arbitrary phase shift, so that the out-going signal is changed.

2.3 Waveguides

Waveguides are structures that can guide waves along its structure[13]. Although it can be used for acoustic waves, it can also be utilized to confine the electric and magnetic energy of an optical wave. This *optical waveguide* structure gives control over the propagation and distance of a traveling electromagnetic wave. The principle behind the confinement of light is that of TIR. There are many types of waveguides, but the one of interest in this work is the *rectangular dielectric waveguide*. Before the relevant waveguide structure can be explained, a more thorough review of the more elementary waveguides has to be conducted.

An electromagnetic wave that propagate through a waveguide can not be a transverse electromagnetic (TEM) wave, which is a result of the boundary conditions derived from Maxwell's equations in Equations 2.9 - 2.12. The electromagnetic wave can either be *transverse electric* (TE) or *transverse magnetic* (TM); determined by whether the electric or magnetic field is oscillating in the x-direction perpendicular to the propagating z-axis, respectively, which is shown in the coordinate system of Figure 2.4. The project will be centered around the propagation of TE waves.

2.3.1 Planer Mirror Waveguide

The planar mirror waveguide is comprised of two parallel planar mirrors separated by a distance d, and is illustrated in Figure 2.4. The mirrors are perfect reflectors and lossless. A wave will propagate along the z-axis as it bounces back and forth through reflections in the two mirrors at an angle θ. The wavenumber, k, describes how the wave propagates through the waveguide and it can be decomposed into a z-component and a y-component[12],

$$
\begin{aligned}
k_z &= nk_0 \cos\theta = \beta \\
k_y &= nk_0 \sin\theta,
\end{aligned}
\tag{2.21}
$$

where β is the *propagation constant* and n is the refractive index.

A monochromatic TE wave with an electric field in the x-axis will be able to propagate through the structure by reflection at the upper and lower planar mirrors.

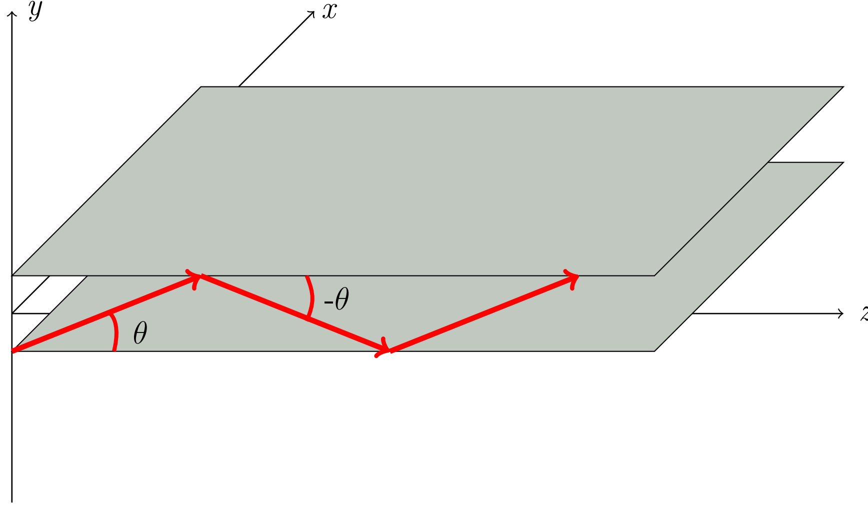

Figure 2.4: Planar mirror waveguide

Compared to a wave that only travels in the z-direction, the TE wave will travel a distance $2d \sin\theta$ further after being reflected twice at the two boundaries. The wave experiences a phase shift equal to $\frac{2\pi}{\lambda} 2d \sin\theta$ as a result to the added distance travelled. additionally, a second contribution to the the wave's phase shift, φ_r, comes from the reflections at the two boundaries. In order to be guided through the waveguide, the wave needs to reproduce itself after two reflections; called the *self-consistency condition*. The condition means that the total phase shift after two reflections must be equal to an integer number of 2π[15], given as

$$\frac{2\pi}{\lambda} 2d \sin\theta - \varphi_r = 2\pi m, \quad m = 1, 2, 3, \ldots. \tag{2.22}$$

For a planar mirror waveguide the second term in Equation 2.22 becomes 2π, thus reducing the aforementioned equation to

$$\sin\theta_m = m\frac{\lambda}{2d} < 1, \quad \rightarrow M = \left\lfloor \frac{2d}{\lambda} \right\rfloor, \tag{2.23}$$

Where M is the total number of modes that the waveguide can support. The modes satisfy the self-consistency condition and will maintain its polarization while propagating through the waveguide. In general, the phase shift φ_r depends both on θ and if the mode is TE or TM polarized[12].

There will also be corresponding wavevectors $\mathbf{k}_m$ for each bounce angle. $\mathbf{k}_m$ can be determined by rewriting Equation 2.21 as

$$\mathbf{k}_m = [0, nk_0 \sin\theta_m, nk0 \cos\theta_m]^T. \tag{2.24}$$

Since the wave propagates in the z-direction, the z-component of the wavevector is the *effective refractive index*. It is dependent on the mode m, and is given by

$$n_{eff,m} = nk_0 \cos\theta_m, \tag{2.25}$$

and is the refractive index that the propagating wave is exposed to.

2.3.2 Planar Dielectric Waveguide

The difference between the planar dielectric waveguide and the perfect mirror waveguide is that the outside of the waveguide is a dielectric material with refractive index n_2. For a wave to be able to propagate through the waveguide, the angle of reflection must be equal to or higher than the *critical angle* θ_c. This is the angle of which TIR occurs within the waveguide, and can been seen in Equation 2.8 when θ_2 reaches 90° and there is no transmission across the boundary.

Another difference is how the wave propagates due to a phase-shift that occurs at the boundary, which is dependent on the two refractive indices. For a TE-wave, this phase shift if given by[15]

$$\varphi_{TE} = 2\arctan\left[\frac{\sqrt{\sin^2\bar{\theta} - (n_2/n_1)}}{\cos\bar{\theta}}\right], \tag{2.26}$$

where $\bar{\theta}$ is the complementary angle of θ, and n_1 and n_2 are the refractive indices of the core and the cladding, respectively, and $n_1 > n_2$.

For an asymmetrical waveguide, e.g. Silicon-on-insulator (SOI) type waveguide, with two different refractive indices at top and bottom, Equation 2.22

$$\frac{2\pi}{\lambda}2d\sin\theta - \varphi_{TE,12} - \varphi_{TE,13} = 2\pi m, \tag{2.27}$$

where indices *i,j* are n_i and n_j in Equation 2.26, respectively. From the aforementioned equation it is clear that two different critical angles will exist in the waveguide, one for each boundary, but it is the largest critical angle of the two that will be the critical angle θ_c of the medium.

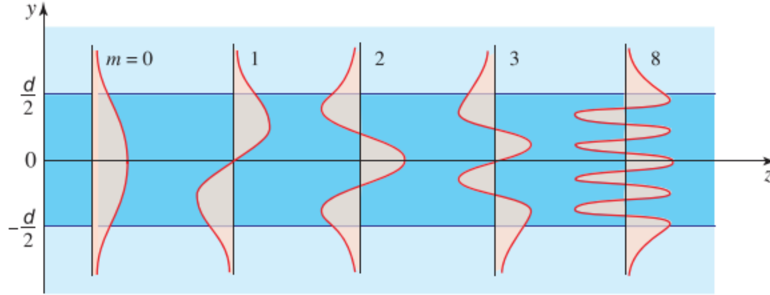

Figure 2.5: Field distribution of the modes in a planar dielectric waveguide. The evanescent field in the waveguide reaches into the dielectric material. The figure is taken from [12].

2.3.3 Rectangular Dielectric Waveguide

A rectangular dielectric waveguide consists of a dielectric rectangular core that is fully or partially covered by a dielectric cladding with a lower refractive index. The preceding elaborated waveguide structure has been considered infinite in the x-direction, but this is not the case for such a rectangular dielectric waveguide. Due to a width that is finite, modes also occur in the x-direction (as opposed to only in the y-direction), and the supported mode in the rectangular waveguide is described by the two indices m and n, resulting in the notation where the TE mode is denoted TE_{mn}.

Both m and n can have a zero value, but not both at the same time, e.g. TE_{01} or TE_{10}. Depending on the geometry of the rectangular waveguide, there exists an optimal TE-mode with the lowest attenuation. This TE-mode is also the mode with the lowest *cut-off frequency*; the lowest frequency that physically can propagate through the waveguide. The cut-off frequency of a rectangular waveguide is given by

$$f_c = \frac{c}{2}\sqrt{(\frac{m}{a})^2 + (\frac{n}{b})^2}, \tag{2.28}$$

where a and b are the width and thickness, respectively. To determine which mode to use during low-loss applications is beneficial. In order to achieve one single mode in the waveguide, the height of the rectangle has to be tailored in such a way that $f_{c,10} < f_{\text{signal}} < f_{c,20}$.

2.3.4 Evanescence and Coupling between Waveguides

From the boundary conditions described by Equations 2.9 and 2.11, the electric field at the boundary is required to be continuous. For a dielectric media the

cladding surrounding the waveguide is not perfectly conducting. Therefore, the field components will exist outside of the waveguide structure. These fields are referred to as *evanescent fields*, and they decay quickly as they reach outside of the waveguide and into the cladding as shown in Figure 2.5.

If there are two waveguides in close proximity, the evanescent fields can reach out and into the adjacent waveguide. Thus, optical power can be transferred between two waveguides if the *coupling distance* is small enough. This coupling effect can be used to create different optical devices such as beamsplitters and optical ring resonators.

Coupled-mode theory is used to describe the physics behind the weak coupling between two waveguides. An assumption is that mode of each waveguide is calculated as an independent system. It is also required that the two waveguides are matched in terms of phase, i.e. they have the same material properties and are single-mode. By taking these two assumptions into account, the input and output amplitudes are related by the transmission matrix, T given by

$$\mathbf{E}_o = T\mathbf{E}_i, \quad T = \begin{bmatrix} A(z) & B(z) \\ C(z) & D(z) \end{bmatrix} = \begin{bmatrix} \cos Cz & -j\sin Cz \\ -j\sin Cz & \cos Cz \end{bmatrix}, \tag{2.29}$$

where $\mathbf{E}_i$ is the input field, $\mathbf{E}_o$ is the output field and C is called the coupling coefficient. The distance needed to transfer all the power from one waveguide to another is called the *coupling length* $L_0 = \pi/2C$. In order to transfer half of the power the coupling length has to be halved. This type of beamsplitting is called a 3 dB coupler, and is used solely in this work.

2.4 Optical Resonators

Optical resonators are devices that are designed to accumulate and confine light at specific *resonant* frequencies. They come in different configurations and with varying properties: the devices can be used as sensors or can even be used as powerful lasers[16]. The simplest form of an optical resonator is the Fabry-Perot resonator, which covers most of the principles in its configuration. However, the *ring resonator* is the most central and relevant component in the MARC device. A brief explanation of the Fabry-Perot resonator will be conducted before preceding to the ring resonator.

2.4.1 Fabry-Perot Resonator

In its 1-dimensional configuration, consisting of two parallel mirrors separated by a distance d, the light is reflected back and forth as optical energy is being stored. This cavity supports certain modal frequencies which are standing waves, similar

to the modes of the parallel-mirror waveguide. Due to the fixed parameter d, the resonant frequencies will have a periodicity with a frequency spacing that is called the *free spectral range* (FSR)[12], given as

$$FSR_\nu = \frac{c_0}{2nd}, \tag{2.30}$$

where n is the refractive index of the medium in the cavity. It is clear that a smaller distance d results in a larger FSR. Distinct resonant frequencies will appear given that the mirrors are perfect. However, losses occur in the resonator, and a broadening of the resonances are introduced. The round-trip attenuation factor, α, is directly correlated with broadening, which is determined by the *finesse*, $\mathcal{F}$, given as

$$\mathcal{F} = \frac{\pi\sqrt{|\alpha|}}{1 - |\alpha|}. \tag{2.31}$$

The width of the resonance peaks is given by

$$\delta\nu \approx \frac{FSR_\nu}{\mathcal{F}}, \tag{2.32}$$

which is only valid in the case where $\mathcal{F} \gg 1$. Since the spectral width $\delta\nu$ is inversely proportional to the finesse $\mathcal{F}$, it follows that an increase in the loss results in an increase in $\delta\nu$.

The *full-width half-maximum* (FWHM) describes the broadness of the peaks given by

$$\text{FWHM} = 2\delta\nu. \tag{2.33}$$

Another important parameter of the resonator is the *quality factor* Q, which is a dimensionless measure of how underdamped the resonating system is in terms of its initial stored energy. It is thus related to the finesse $\mathcal{F}$ through the approximation

$$Q \approx \frac{\nu_0}{\nu_F}\mathcal{F}, \tag{2.34}$$

where ν_0 is the resonance frequency. Since ν_0 typically is much greater than $\mathcal{F}$, we have that Q $\gg \mathcal{F}$.

2.4.2 Ring Resonator

The ring resonator is a closed-loop circular waveguide capable of sustaining specific resonant frequencies. The different parameters of the ring resonator determine which frequencies that can resonate within the device. The ring resonator can be coupled with a single straight waveguide to couple light. This configuration is called an *all-pass* ring resonator, and exhibits filtering characteristics[12, 17].

All-Pass Ring Resonator

A few assumptions of the all-pass ring resonator are that the coupling is lossless, only one single mode in the resonator is present, only a single polarization is considered and the attenuation constant α is all the loss through a round-trip in the ring resonator.

If these assumptions are fulfilled, the coupling in the ring resonator can be described similarly to that of Equation 2.29. For the all-pass ring resonator, the coupling is described by[17]

$$\begin{bmatrix} E_{o1} \\ E_{o2} \end{bmatrix} = \begin{bmatrix} t & \kappa \\ -k^* & t^* \end{bmatrix} \begin{bmatrix} E_{i1} \\ E_{i2} \end{bmatrix}, \tag{2.35}$$

where κ is the complex coupling parameter describing the coupling from the ring resonator to the straight waveguide (κ^* is the complex conjugate of κ) and t describes the self-coupling of the waveguides (t^* being the conjugate). The coupling parameters need to satisfy $|k|^2 + |t|^2 = 1$ due to symmetry of the matrix in Equation 2.35.

The round-trip attenuation, α, is described as the propagation loss of light propagating one trip around the ring resonator, and can be seen in the relation

$$E_{i2} = \alpha e^{j\phi} E_{o2}, \tag{2.36}$$

where $\phi = n_{eff} k_0 2\pi r$, n_{eff} is the effective refractive index of the ring resonator and r is the radius of ring resonator.

However, the transmission of the electric field from the waveguide into the ring resonator is an important part of the structure. By combining Equation 2.36 with Equation 2.35, we get the following expression

$$E_{o2} = \frac{-\alpha + t e^{-j\phi}}{-\alpha t^* + e^{-j\phi}} E_{i1}, \tag{2.37}$$

In order to get a maximum signal at resonance, the loss in the ring has to equal the coupling loss, i.e. $\alpha = |t|$; resulting in zero intensity transmission at resonance. This

phenomenon is called *critical coupling* and is the result of destructive interference between the field in the bus-waveguide and the field that is coupled back into the waveguide from the ring resonator.

Add-Drop Ring Resonator

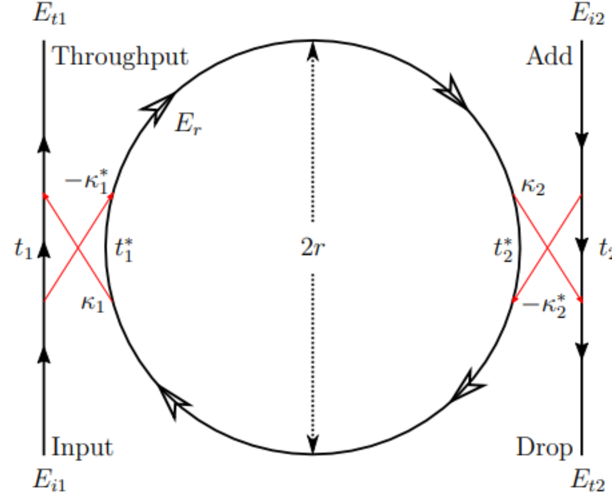

Figure 2.6: An illustration of the add-drop ring resonator with a given radius r The 4 different ports (add, drop, through, and input) are shown. The red lines are where the coupling between the waveguide and the ring resonator occurs.

An add-drop ring resonator is a more complex device, but builds on the same principles as the all-pass ring resonator. The device have another added waveguide coupled to the ring resonator, so that the configuration have four ports (input-, through-, add-, and drop-ports) as shown in Figure 2.6. At resonance a signal can be coupled into the through-port signal via the add-port, and at the same time it can be coupled out of the input-port via the drop-port.

For simplifications $E_{i1} = 1$. It is assumed that there is no input at the add-port. The electric field at the through-port is then given by[17]

$$E_{o1} = \frac{t_1 - t_2^* \alpha e^{j\varphi}}{1 - t_1^* t_2^* \alpha e^{j\varphi}}. \tag{2.38}$$

For the the drop-port the electric field is given by

$$E_{o2} = \frac{-\kappa_1^* \kappa_2 \alpha_{\frac{1}{2}} e^{j\varphi_{\frac{1}{2}}}}{1 - t_1^* t_2^* \alpha e^{j\varphi}}, \tag{2.39}$$

where $\alpha_{\frac{1}{2}}$ and $\varphi_{\frac{1}{2}}$ are the loss and phase delay after half a round trip in the ring resonator, respectively. In order to get the strongest signal, i.e. maximum intensity at resonance, the two parameters t_1 and t_2 have to fulfill the relation

$$\alpha = \left|\frac{t_1}{t_2}\right|, \tag{2.40}$$

which is the principle of critical coupling. When analyzing the output signal, the resonance frequencies are recognized by the distinct periodic peaks. The distance that separates these peaks is the same free spectral range as in Equation 2.30 for the Fabry-Perot resonator. However, for the add-drop ring resonator the free spectral range is given by

$$FSR_\lambda \approx \frac{\lambda_0^2}{n_{eff}L}, \tag{2.41}$$

where $L = 2\pi r$ is the length of the ring. It is assumed that n_{eff} is not a function of FSR_λ, i.e. dispersionless.

Finally, Equation 2.41 can be used to determine an expression for the Q-factor

$$Q = \frac{n_{eff}L}{\lambda_0}\mathcal{F}, \tag{2.42}$$

where $\mathcal{F} = \mathrm{FSR}_\lambda/\mathrm{FWHM}_\lambda$.

Non-Parallel Add-Drop Ring Resonator

The two waveguides that are coupled to the ring resonator do not have to be parallel. By changing the direction of the drop-port, the configuration of the two waveguides can be described by an angular separation θ as shown in Figure 2.7. The electric field at the drop-port is given by[17]

$$E_{o2} = -\frac{\sqrt{1-t_1^2}\sqrt{1-t_2^2}\alpha_\theta e^{j\varphi_\theta}}{1-t_1t_2\alpha e^{j\varphi}}. \tag{2.43}$$

When the coupling is identical at the two waveguides, i.e. $t = t_1 = t_2 \in \mathbb{R}$, Equation 2.43 simplifies to

$$E_{o2} = -\frac{(1-t^2)\alpha_\theta e^{j\varphi_\theta}}{1-t_1t_2\alpha e_{j\varphi}}, \tag{2.44}$$

where $\alpha_\theta = \alpha^{\theta/360°}$ and $\varphi_\theta = \varphi \cdot \frac{\theta}{360°}$.

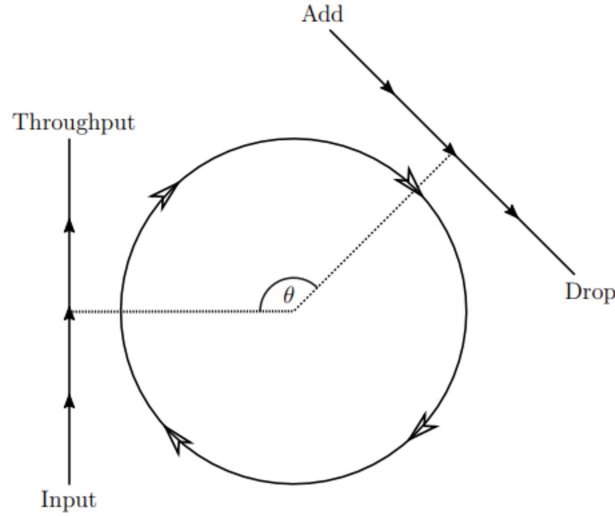

Figure 2.7: Non-parallel add-drop ring resonator with an arbitrary angular separation θ. This configuration will be the one used to design the MARC sensors in this project.

Changing the angular separation gives a different transmission response compared to the parallel add-drop ring resonator.the main difference between the various configurations altered by the angular separation, is the difference in phase accumulation between the resonances. For the parallel add-drop ring resonator, the phase accumulated between two resonances is π. The accumulated phase between resonances is in fact equal to the angular separation. The phase of the transmitted signal at the output of the drop-port is mathematically described as

$$\phi = \arctan \frac{Im\{E_{o2}\}}{Re\{E_{o2}\}} = \pi + \varphi \frac{\theta}{2\pi} + \arctan \frac{t_1 t_2 \sin \varphi}{1 - t_1 t_2 \alpha \cos \varphi}. \tag{2.45}$$

This phase response is the key role in how the MARC device can function as a sensor.

2.5 MARC Device

A *Mach-Zehnder interferometer-assisted ring resonator configuration* (MARC) device is comprised of a balanced Mach-Zehnder interferometer and a given number of ring resonators in the phase-shifting arm[2]. The angular separation(s) is arbitrary for the ring resonator(s), and contributes to the transmitted signal of the device.

By combining the angular separation and radius of each ring, the signal can be altered to be of a certain shape. This increases the device's sensing range and makes it possible to add more ring resonators to the device without distorting the signal.

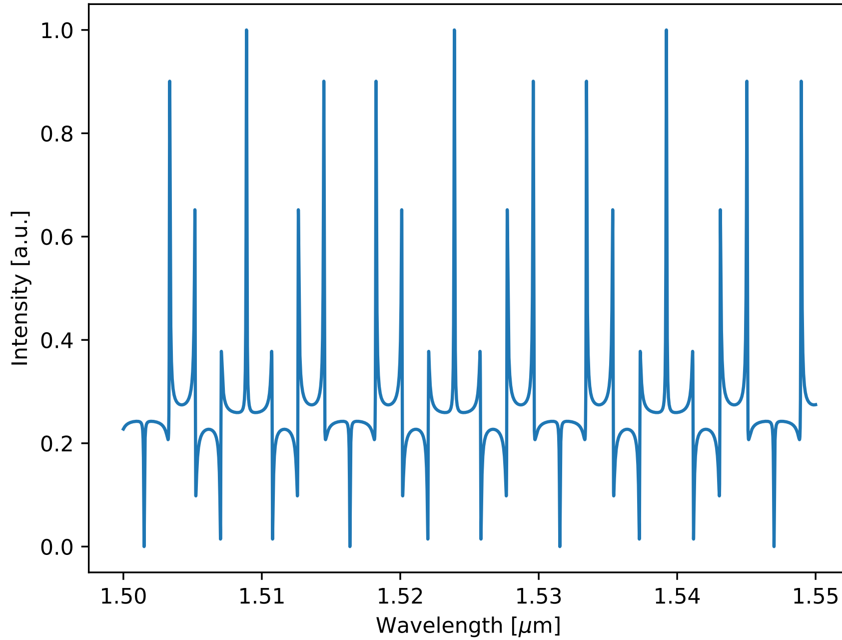

Figure 2.8: The theoretical transmission spectrum of a MARC device with radius 50 μm and angular separation of 135°.

The simplest MARC device consists of one single, lossless (i.e. $\alpha = 1$), critically coupled (i.e. $t_1 = t_2$) ring resonator with an arbitrary angular separation. The interferometer arms are split by a beamsplitter, where one of the arms is regarded as the balancing arm. The other interferometer arm is connected to the non-parallel add-drop ring resonator. Then the ring resonator is connected back with the balancing arm through the drop-port.

To find the transmitted intensity of the MARC device, Equation 2.19 can be solved, yielding[3]

$$I = \frac{1}{4}(1 + |E_{o2}|^2 + 2|E_{o2}|\cos\phi), \tag{2.46}$$

where the phase shift ϕ is assumed to be the expression derived in Equation 2.45. It is also assumed that the intensity in the balancing arm I_1 is equal to one to simplify the intensity expression. The MARC device will convert any phase shift from the ring resonator into a detectable transmitted intensity response. A plot for a MARC device with an angular separation of 90° is shown in Figure 2.8

When the accumulated phase reaches an integer multiple of 2π the transmission spectrum repeats itself. The transmission spectrum has a periodicity, which is defined as the *effective free spectral range* (FSR_e). The FSR_e is related to the free spectral range, as the name suggests, and the relation is given by

$$FSR_e = N \cdot FSR, \tag{2.47}$$

where N is given by θ as

$$\theta = 2\pi \frac{M}{N}, \tag{2.48}$$

where $M/N = L$. L can have two different values depending on the angular separation of the configuration, where L can either be a rational number or a positive integer. If L is a rational number, then L is given as an irreducible fraction $L = M/N$. In the other case where L is a positive integer, then $L = N$ because $M = 1$.

2.5.1 Spectral Line Shapes

When passing a interval range of wavelengths through the MARC device it creates an output transmission spectrum which depends on the geometry of the add-drop ring resonator. This spectrum can be considered a finger print of the device, as it is unique for the geometrical structure. In resonators it is common to detect both a symmetrical *Lorentzian* line shape and an inverse *Lorentzian* line shape which both have a unique shape. The Lorentzian line shape appears when there is photon absorption/emission and in resonators[12].

However, in the resonating MARC device an *asymmetric Fano* line shape also occurs when the angular separation deviates from the standard 180° configuration, i.e. a non-parallel add-drop ring resonator. The latter line shape is not common in conventional resonators, and arises from the constructive and destructive interference of a discrete quantum state with a continuum band of states. This also explains why asymmetric Fano line shapes does occur in conventional ring resonators. In the MARC device the Fano line shape occurs because of scattering in both the balancing arm that is non-resonant broadband and in the phase-shifting arm that is narrowband resonant.

The Fano line shape is given by

$$\sigma(\omega) = D^2 \frac{(q + \Omega)^2}{1 + \Omega^2}, \tag{2.49}$$

where $q = \cot(\phi/2)$ is the asymmetry factor, ω is the angular frequency, $D = 2\sin(\phi/2)$ is the scaling factor, ϕ is the phase shift, and $\Omega = 2(\omega - omega_0)/\gamma$ is the reduced frequency, where γ and ω_0 are the resonance width and frequency, respectively.

2.5.2 Multiplexed MARC Device

A stand-alone MARC sensor consists of a single add-drop ring resonator, but it is possible to combine several MARC sensors into one device. This a what is called multiplexing, by combining two or more signals into the same signal. The parameters, e.g. radius, angular separation, of the individual ring resonators determine the transmission spectrum of the multiplexed MARC sensor. It is this sensor that is the main focus of this project. The multiplexed MARC sensor that is used in this project is shown in Figure 4.1.

2.5.3 MARC Device as Sensor

The optical path length of a waveguide depends on the refractive index (see Equation 2.21), meaning if there is any alteration to the refractive index, there will be a change in the optical path of the optical wave. This means that the resonant peak in a ring resonator will shift, since there will different wavelengths that undergoes constructive and destructive interference. By measuring this resonant wavelength shift, it is possible to determine the external forces that contributed to this. Such external forces could be temperature, an applied field, or the presence of a biological analyt[2]. The latter is what is used to turn the MARC device into a biological label-free sensor.

3 | Methods

The methods used in this project will be described in this chapter. The programming language *Python 3.11* (Python) was used to calculate the transmission spectrum of an ideal MARC sensor. Python was also used to process the data and create plots of the data.

The MARC device was simulated using the program *COMSOL Multiphysics 6.0* (COMSOL), which is a so-called finite-elements method (FEM) software. Different modules that contain the theoretical information about the physics, e.g. wave optics, can be combined together to tailor the physical situation for the desired simulation. This makes COMSOL capable of modeling and solving various physical problems with varying complexity. The software is a powerful tool to simulate real physical problems if the model is created correctly.

The experimental methods were conducted at Nanolab and at a dedicated laser lab, both at NTNU. The working principles of the various fabrication and characterization tools will be explained.

3.1 Theoretical framework

Python[1] has been used to process the simulation data and present it using the Python package *Matplotlib*. The plot presents the measured intensity over a given wavelength spectrum, and is the same measurable quantity used for the physical MARC sensor.

Also a theoretical MARC sensor has been simulated in Python using simple calculations. These calculations are fast, and were mainly used to gain insight into how the sensor would function with various configurations. This determined the different radii and angular separations used in the multiplexed configuration, so that the multiplexed intensity signal could easily be broken down into it's individual sections. Three different intensity signals are shown in Figure 5.7 together with the combined

[1]https://www.python.org/

signal, i.e. multiplexed signal of the individual signals. The script is based of on the work of Yadav et. al [2], which was done in Matlab[2].

The ideal simulations are given an input intensity with amplitude $E_i = 1$ V/m and phase $\varphi = 0$. The output intensities of the ring resonator at the through-port and drop-port are calculated using Equations 2.43 and 2.44. The through-port output from one ring resonator is used as the input for the next ring, which makes it possible to cascade ring resonators to create a multiplexed MARC sensor. The drop-port output from each ring is added up and summed together before calculating the intensity from Equation 2.19. The phase difference is zero due to the ideal conditions of the calculations. However by introducing a phase difference it is possible to see how an unbalanced MARC sensor behaves.

The parameters of the MARC sensor can be adjusted (i.e. ring resonator radius, wavelength spectrum, n_{eff}, angular separation, self-coupling coefficient etc.). However, one of the limitations of the Python simulations are the ideal conditions, i.e. the waveguide structures are critically coupled and there are no unwanted reflections occurring in the structure. There are no wavelength dependencies and no phase delay in the beamsplitter. These perfect conditions are not an accurate depiction of the physical MARC sensor, but it provides valuable insight into how the structure behaves. Several factors can results in a distorted signal when fabricating the sensor, such as impurities, wrong fabrication parameters etc. With the knowledge of how an ideal sensor behaves, it makes it possible to determine if the fabrication process is done correctly.

3.2 COMSOL Simulations

The geometry made in COMSOL to carry out the different simulations for the MARC sensors are shown in Figure 3.3.

Before starting to create the geometry that will be subjected to the physical simulation, the *Space dimensions* of the model have to be selected. This can either be from zero to three dimensions or axiosymmetric 1D/2D.

Furthermore the *Physics* of the model have to be defined. There are a wide variety of different modules covered by COMSOL, e.g. Electrochemisty, Semiconductor, Multibody Dynamics. It is possible to select several modules, and once one (or more) physics modules have been selected the user also has to select a *Study*. This determines the set of equations that will be solved while running the simulations.

After all the physical selections are chosen, the *Parameters* of the system can be manually added to a parameter list. This includes different information to perform the simulations, e.g. refractive index of materials, height of geometry, wavelength

[2]https://www.mathworks.com/products/matlab.html

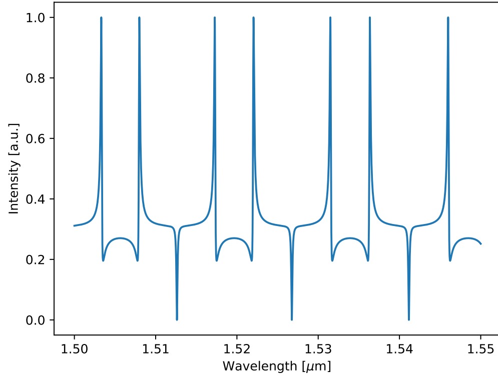

(a) Theoretical transmission spectrum of a MARC sensor with an angular separation of 240° and with a ring radius of 20 μm. FSR_e = 21.5 nm.

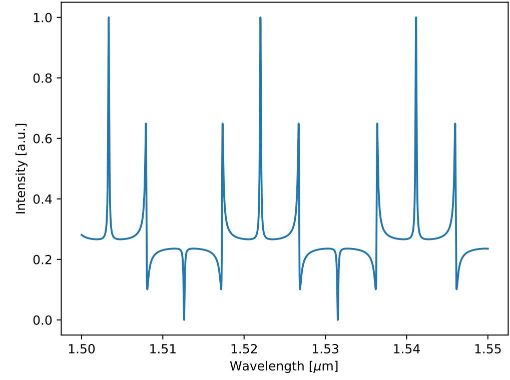

(b) Theoretical transmission spectrum of a MARC sensor with an angular separation of 90° and with a ring radius of 25 μm. FSR_e = 22.9 nm.

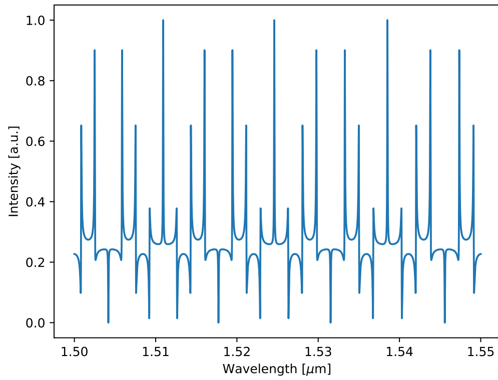

(c) Theoretical transmission spectrum of a MARC sensor with an angular separation of 135° and with a ring radius of 55 μm. FSR_e = 20.8 nm.

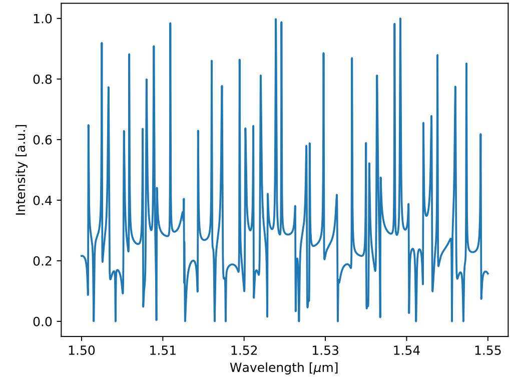

(d) Multiplexed MARC sensor with three ring resonators of radii 20 μ, 25 μm, and 55 μm with an angular separation of 135°, 90°, and 240°, respectively. The signal is mixed, but the peaks from the individual signals in a), b), and c) are still present and observable.

Figure 3.1: The transmission spectrum based on the work of Yadav et al. [2]. These figures are all theoretical, and are created in an idealistic system.

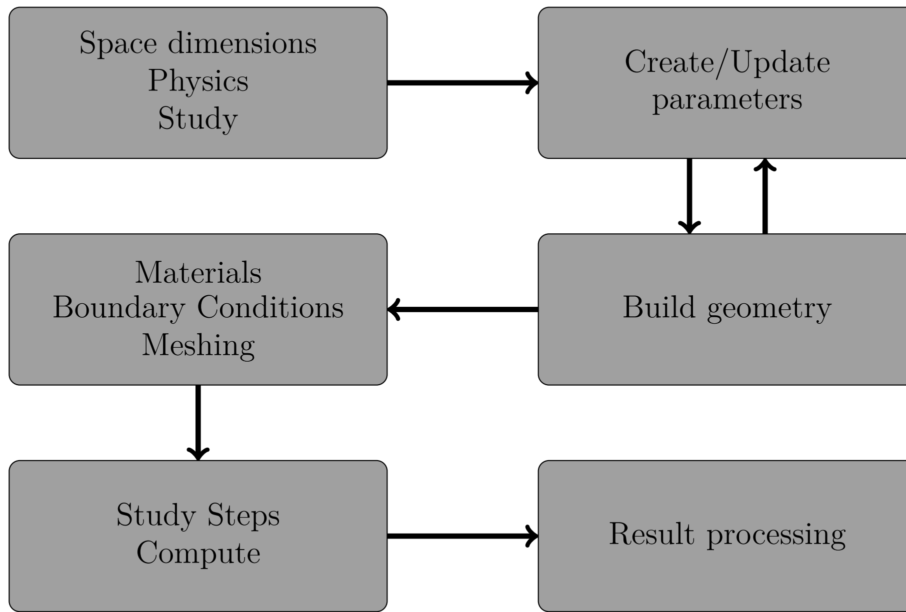

Figure 3.2: Flow chart of how to use COMSOL. The dimensions, physics to be used, and what to study are set. Then the parameters that will be used for the geometry, e.g. thickness, are defined. When the geometry is built, the materials, boundary conditions are specified, Perfectly Matched Layers and the mesh is added to the design. Then the study steps are chosen and the design is simulated. Once the simulation is done the results can be processed.

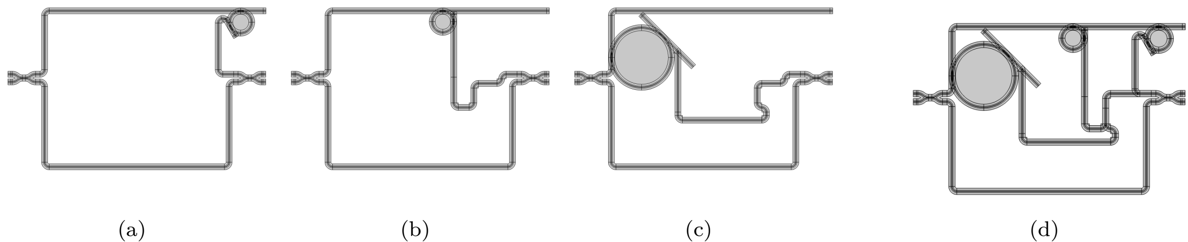

(a) (b) (c) (d)

Figure 3.3: a) COMSOL model of a MARC sensor with angular separation of 240°, b) COMSOL model of a MARC sensor with angular separation of 90°, c) COMSOL model of a MARC sensor with angular separation of 135°.

used to simulate the input laser. The value of the parameter can be of any numerical value and unit. Note that the parameters can be added to the parameter list at any point during the building process of the model, and is more of a tool rather than a necessity.

To build the *Geometry* of the model, the software uses a computer-aided design approach. This includes making precise components within a coordinate system with specifications of size and placement. It is also possible to divide the component into different sections through the use of the *layer* function. Each *Boundary* (line) and *Domain* (area within lines) are labeled in the software.

Figure 3.4: Effective mode index setup. The model is a 10 μm long structure, with a 1 μm thick SiO_2 layer on the bottom layer and a 220 nm thick waveguide of Si on the top layer. The air layer is 2 μm thick.

Once the geometry is built, different material properties can be assigned to the different domains, e.g. Si to the core and SiO_2 to the cladding of the waveguide. COMSOL provides the user with a library of different materials, but it is also possible to customize a material with respect to the refractive index, heat capacity, etc.

The boundary conditions need to be applied to the designed geometry. This depends on both the *Physics* and *Study*. This reduces the computational time if the *Perfectly matched layers* (PML) are applied correctly. The PML mimics an open and non-reflecting domain – the domain absorbs any electric field incident on it. Another boundary condition that can be applied is input/output ports that either generate power or absorb power.

Before the software can execute the simulation, the geometry of the model has to be divided into smaller elements. Ideally each element should be small enough so that the relevant physics will behave linearly. This is the FEM approach, and contributes to simplify the simulation. The process of tessellation is called *Meshing*, and is a critical step prior to carrying out the simulation. A rule-of-thumb is that the more complex the geometry is, the finer the mesh is required to be.

Finally the solution to the simulation has to be created, usually defined by the *Study* selected earlier. However, it is also possible for the user to select different *Study steps*, such as a parametric sweep which repeats the simulation while changing a selected parameter over a user-defined range. The results are displayed in different default plots, but the data from the simulation can be exported from COMSOL as a file, e.g. csv.-file.

3.2.1 Effective Mode Index Analysis

Three-dimensional simulations require a lot of computational power, and it is therefore desirable to simulate in two-dimensional space. When doing two-dimensional simulation the model is created from a top-down perspective, but it requires that one of the axes is assumed to be infinite. A preliminary simulation has to be performed

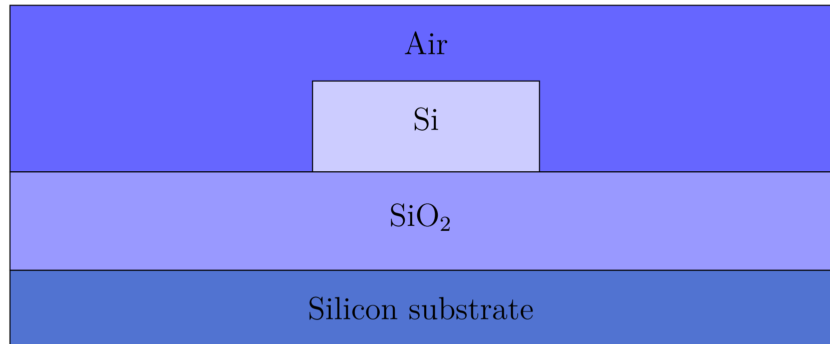

Figure 3.5: Effective mode index setup viewed from the front.

in order to gain valuable information about the dimension that will be neglected in the two-dimensional simulation.

Figure 3.4 and Figure 3.5 shows the setup for the effective mode index analysis from the side and front perspective, respectively. The system is a vertical slab with three layers: the substrate, the waveguide, and the top cladding being viewed from the side. Each of the layers is assigned its respective refractive index. Then an analysis is carried out on the system, which is done by selecting the *Study* called *Mode Analysis*. Here the frequency and desired number of modes are selected. The value of the *effective refractive index* can now be used to simulate a two-dimensional structure as if it were a three-dimensional structure, but having a "top-down" view. This method is often used when analysing waveguides, so that the computational power needed is reduced [18].

Preferably the electric field that propagates through the core should be confined, not entering into the top and bottom layer of the slab. When conducting the effective mode index analysis, it is convenient to make an assumption of what value the effective refractive index will have. This will give the simulation a better starting point when looking for the effective refractive index. Since the core will have a refractive index higher than both of the two layers, most of the electric field will be confined inside the core. Thus, the effective refractive index will take a value closer to the refractive index of the core rather than the refractive index of the surrounding layers.

3.3 Fabrication

Several fabrication tools are used during the fabrication process of creating the MARC sensor and the polymer waveguides used for optical fiber-coupling. Some tools are rather simple to use and understand, while other tools need a more thorough explanation to comprehend. This section will present the main tools used in the fabrication of the MARC sensor. The more trivial equipment such as hot

plates, plasma cleaners, spin coaters, ultrasonic baths and scribing tools will not be elaborated on in this section. However, a more detailed outline of all the tools and parameters used during the fabrication process are listed in Section **??**.

3.3.1 Silicon-on-Insulator

Silicon-on-insulator (SOI) has gain attraction as the material of choice when creating photonic devices [19]. This is due to crystalline silicon (c-Si) having low absorption around the 1500 nm frequency band. Also there is a strong light confinement between Si and SiO_2 as a result of the big contrast in refractive index between the two materials. The SOI technology is compatible with the CMOS technology that dominates the semiconductor industry.

A schematic of how the layers in the SOI system is seen in Figure 3.4. A thickness of 220 nm of the silicon layer gives a single mode for each of the polarization (TE and TM, see Section 2.3.3) around the 1.0 GHz frequency band [19]. The thickness of the SiO_2 layer depends on which type of mode that is being used. TE modes are well confined if the cladding have a thickness of around 1 μm, which is enough to avoid leakage of the optical power. Typically TM modes are confined if the thickness is close to 3 μm.

The SOI system have a disadvantages since the silicon is an indirect bandgap semiconductor. The result is that the silicon can not be used for conventional light generation. Moreover, there are fabrication induced roughnesses as a result of the dense circuitry coming from the high index contrast between Si and SiO_2 [20]. This results in scattering losses, since the sidewalls in the waveguide are not smooth. There is also a question of cost when using SOI wafers. Due to the challenging manufacturing process that increases the cost, there are viable options that suffice when experimenting on a photonic structure [19].

Amorphous silicon (a-Si) can be used as the top layer instead of c-Si. This layer can be deposited on a thermally oxidized silicon wafer, and can be done using e.g. PECVD. Growing a-Si using PECVD is the fabrication method used in this project, mainly due to the low cost and readily availability. This fabrication method is usual when developing SOI photonic systems, because the results are similar to c-Si [21].

3.3.2 Plasma-Enhanced Chemical Vapor Deposition

Chemical Vapor Deposition (CVD) is a process where a thin film is deposited on to a wafer substrate through a chemical reaction using a gas mixture [23]. The wafer substrate is heated up to a goal temperature, so that the chemical reaction occurs at a desired speed.

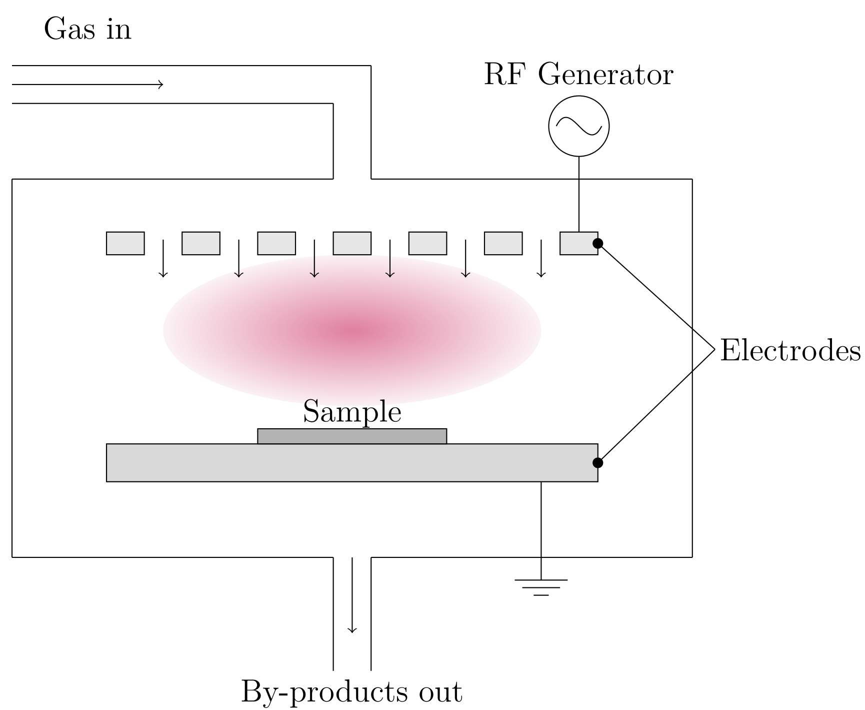

Figure 3.6: Schematic of PECVD. The inlet gasses enters the chamber, where a plasma is created in an applied RF field. Then a thin film is created through chemical reactions on the sample surface. Figure is adapted from [22]

The precursor gas comes from an external source, and a chemical reaction between the different gases creates a thin film deposited on the substrate surface. Plasma-Enhanced CVD (PECVD) is a type of CVD process, which involves converting the precursor gases to plasma [24]. By utilizing plasma as a chemical stimulus, the temperature requirement is lowered to around 300-400°C, considerably lower temperature than what is required for a CVD process.

A schematic of how to PECVD works can be seen in Figure 3.6. The plasma is created between two electrodes by applying a radio frequency (RF) field, which converts energy to the plasma through induction coils. The species formed in the plasma reacts with the surface of the sample and deposits a film [24].

Several physical parameters determines the properties of the thin film. This includes the temperature of the substrate, power/frequency of the RF field, gas compositions, pressure, and flow rate. Utilizing PECVD for thin film deposition yields good adhesion and a low deposition temperature.

PECVD: Amorphous Silicon Film Deposition

For the MARC sensor, PECVD is used to deposit an amorphous silicon (a-Si) thin film layer on a thermally oxidized wafer. The precursor gases used are silane (SiH_4) and argon (Ar) due to availability in the lab. The chemistry that occurs during the thin film deposition is rather complex, it can be described by the simple reaction equation between SiH_4 and Ar, namely

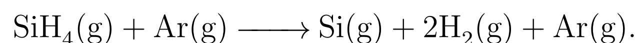

$$\mathrm{SiH_4(g) + Ar(g) \longrightarrow Si(g) + 2H_2(g) + Ar(g).}$$

Due to the inherent nature of dangling bonds in a-Si, the thin film are exposed to defects from the uneven crystalline network. However, the incorporation of hydrogen reduces the defect state of the thin film through passivation [47]. This does result in lower losses during propagation of light through the waveguide structure. The hydrogen is introduced into the thin film from the gaseous by-product H_2.

3.3.3 Electron Beam Lithography

Electron Beam Lithography (EBL) is a lithography technique where an electron beam scans over a resist material to imprint a pattern on to the sample [25]. This technique yields a sub-10 nm resolution, but there is also a sacrifice of a low throughput. Hence, a long exposure time is common for EBL, which limits the amount of MARC sensors that can be experimented on. Exposure times exceeding 12 hours are to be expected for complex structures.

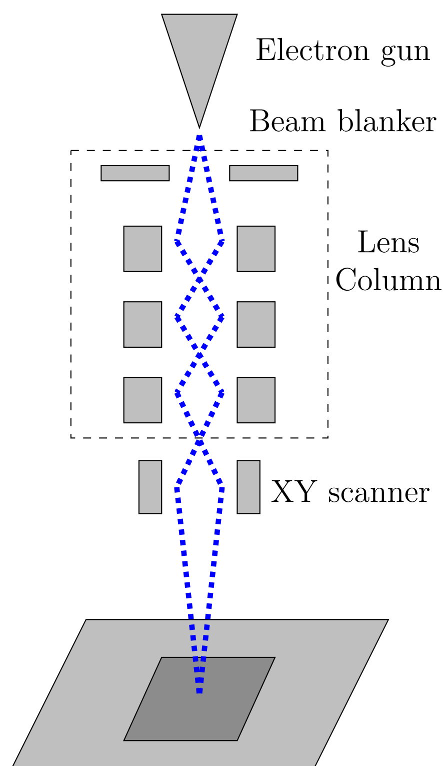

Figure 3.7: Schematic of EBL. The electron beam is created in the electron gun, where it is focused by passing through the lens column. The XY scanner deflects the beam, which operates over a given write field. When the sample is moving, so that a new area is exposed to the write field, the beam blanker stops the electron beam from exposing the sample. Figure adapter from [27].

Due to the high focus that is achieved, patterns at nano-scale can be created with high precision. Since the EBL uses a scanning mechanism, there is no need for a physical mask, making is easier to create a digital mask prior to exposure.

The e-beam resist's solubility, similar to that of a photoresist, is highly dependent on the amount of exposure to the electron beam, which makes it important to ensure a homogeneous distribution of electrons [26]. Due to primary electrons being scattered, i.e. backscattering, the dose distribution is wider than the mask pattern. This results in an uncertainty in the pattern. However, by taking the so-called proximity effect into consideration, a different dose distribution throughout the mask pattern can ensure uniformity in the solubility of the e-beam resist. An illustration of what happens if the proximity effects are not taken into consideration is shown in Figure 3.9.

Pre-Exposure

Prior to exposure a few essential steps need to be followed in order to ensure good adhesion between the substrate and resist, and to make sure there are no contaminants

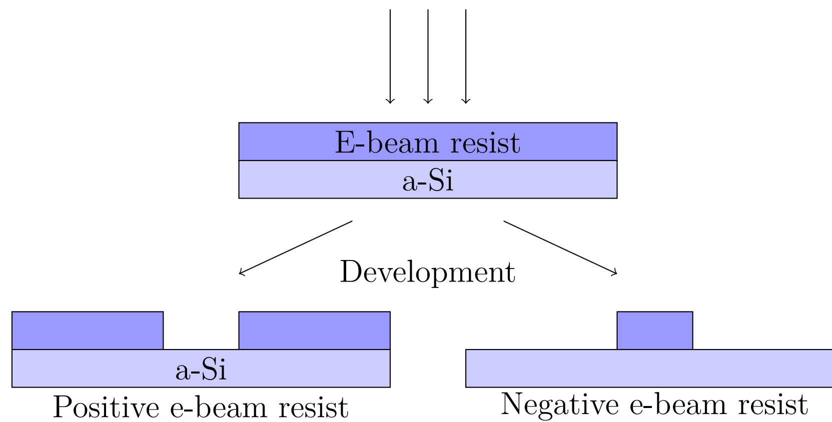

Figure 3.8: Illustration of how positive and negative e-beam resist develops.

on the substrate surface. Acetone and isopropyl alcohol (IPA) are normally used to clean the surface of the substrate, and to ensure a thorough cleaning process, the implementation of an ultrasonic bath can be included.

Specialized e-beam resist is dispersed on the wafer surface in a uniform layer, usually through the use of a spin coater. A set of parameters are determined to achieve the desired thickness of the resist. These parameters are the spin speed, the spin acceleration, and the spin duration, which influence the thickness of the resist. However, the viscosity of the e-beam resist can be a limiting factor to achieve the desired thickness.

An illustration of how a positive and a negative e-beam resist works can be seen in Figure 3.8. A positive e-beam resist will become soluble upon exposure, so that the mask pattern is printed onto the resist. If the e-beam resist is negative, i.e. becomes insoluble upon exposure, the mask pattern will be opposite of the printed pattern.

Following the spin coating, there is a soft bake performed on the wafer. This usually includes the use of a hot plate, where the temperature and duration are determined based on the type of resist used. The soft bake is performed to drive off the solvent in the resist, but it also results in better substrate-resist adhesion.

Exposure

The sample is loaded into the EBL chamber, where it is mounted on the sample holder. Once this is done, a set of parameters for the EBL exposure is chosen. This includes beam current, beam diameter, both beam focus and beam stigmatization, exposure dose, and the write size field. Recall from Section 3.3.3 that a higher beam current decreases the exposure time, but it also decreases the resolution of the beam. Most parameters do not have to be exact, especially if the design does not require

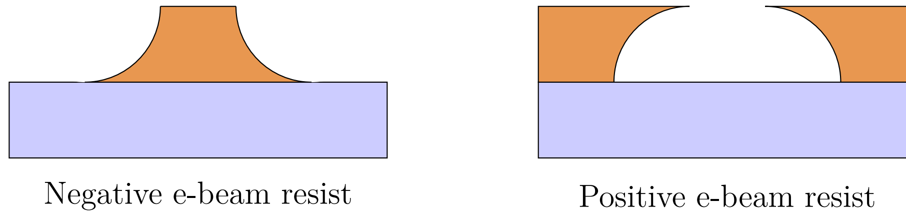

Figure 3.9: Illustration of how the proximity effect from the EBL exposure affects the intended pattern. Straight, rectangular patterns are desired.

very high resolution.

However, a parameter that requires accuracy is the exposure dosage. Too high exposure can lead to an inaccurate design that is too wide (or even rendering out coupling areas between waveguides). If the exposure dosage is too low, the resist can be under-exposed and the resolution might be too low for the design to function properly. A dose test is usually conducted in a systematized manner prior to the exposure, in order to determine the optimal dose for the given design.

Once the parameters of the exposure are set, the mask pattern is then placed in the software of the EBL. The mask pattern is given coordinates, which coincides with the sample holder's coordinates. Then the exposure of the e-beam resist can begin.

Post-Exposure

When the exposure is done, the sample has to be developed. This step will remove the part of the e-beam resist that did not become insoluble during exposure. This step requires the use of a developer, and is usually accompanied by the use of a liquid that dilutes the developer after development (e.g. water or IPA). When the sample is dried out and ready to proceed to the next step of the fabrication, an inspection in an optical microscope is done to verify that the structure is intact and up to standard. An electron microscope (e.g. Scanning electron microscopy) can be utilized if the sample is conducting. Otherwise an optical microscope should suffice.

3.3.4 Inductively Coupled Plasma-Reactive Ion Etching

Reactive Ion Etching (RIE) is an etching technique that results in a directional anisotropic etch on the substrate surface as a result of chemically reactive plasma [28]. The ions accelerate in a directional electric field in combination with chemical processes in a reactor chamber, which is the reason for the anisotropicity.

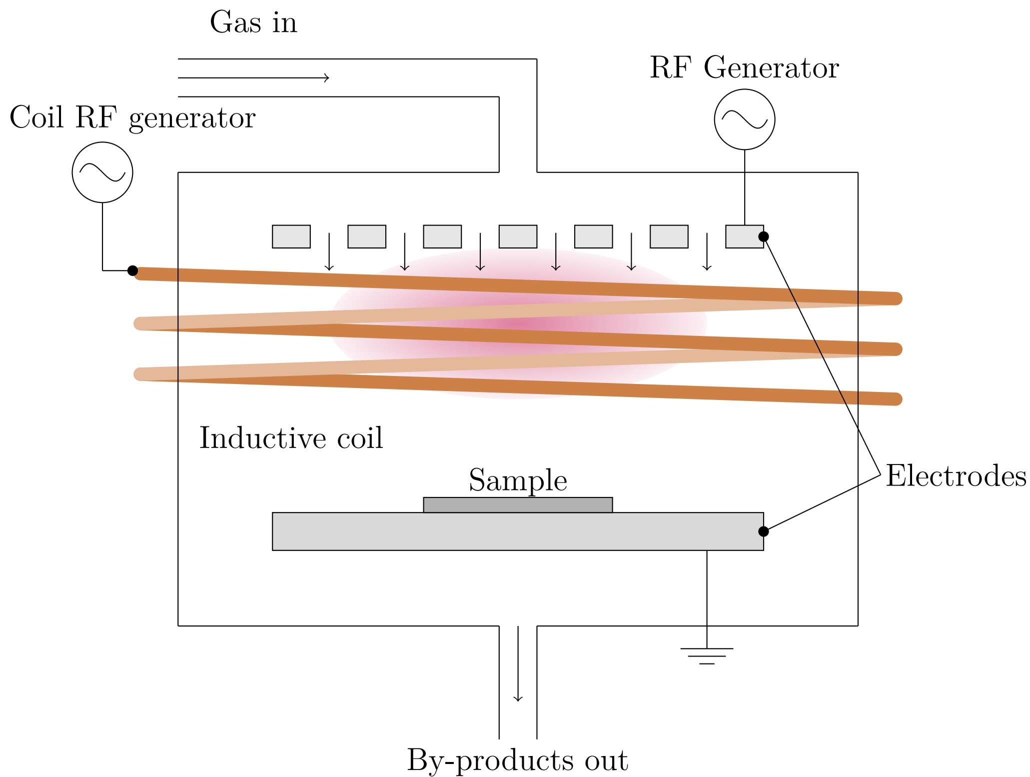

Figure 3.10: Schematic of ICP-RIE. The plasma is created from the inductive coils, and is accelerated towards the sample. This results in an anisotropical etch. Figure adapter from [31]

Inductively-Coupled Plasma-Reactive Ion Etching (ICP-RIE) is a type of RIE system where the plasma is generated from an inductive coil connected to a RF generator. The process chamber of the ICP-RIE can be seen in Figure 3.10. The plasma is created from the gases being excited from a magnetic field created by the RF generator. Due to the bias being created between the electrodes, the plasma is transported towards the sample surface. ICP-RIE is capable of achieving a high plasma density, which in turn will result in a high etch rate. The plasma can consist of various gases, but fluorine-based gases (e.g. CHF_3 and SF_6) are common for etching of silicon based structures [23].

The amount of total surface area on the sample will influence the etch rate and and etch depth of the ICP-RIE process. This phenomenon is called the *loading effect*, and occurs because a larger sample (i.e. larger etchable surface) will deplete the reactants from the plasma faster compared to a small sample. By keeping the surface relatively constant, this problem can be alleviated [29, 30].

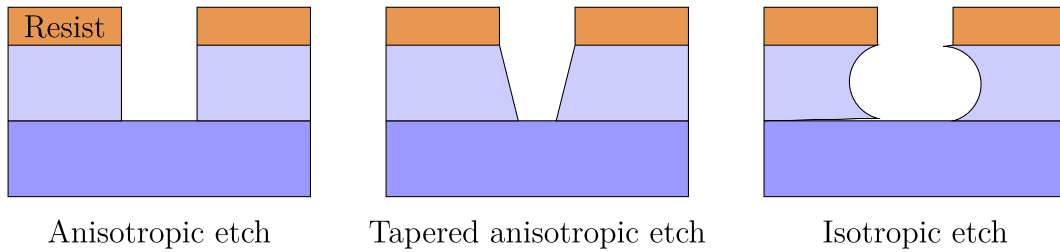

Figure 3.11: Typical profiles of the sidewalls that can be created with different types of etching. Figure is adapted from [32].

3.3.5 Photolitography

Photolitography is conceptually very similar to that of the EBL, but uses photons instead of electrons. The photoresist is exposed to near-UV light (365 nm for i-line photolitography), which results in a limitation of 0.365 μm in resolution [23].

However, photolitography does have it's advantages despite the low resolution. Since it is not dependent upon a single beam (like the EBL), it can illuminate the entire wafer at the same time. This drastically reduces the exposure time by several magnitudes compared to that of the EBL [33].

3.4 Characterization Tools

During and after the fabrication process, it is useful to inspect and characterize the sample. Not only does it indicate if something has gone terribly wrong, which can easily happen, but it also functions as a quality control. If something has gone wrong during one of the fabrication steps, it does not mean that the entire sample is ruined and that the process has to restarted. Often times it is possible to go back to where it went wrong, and then proceed again. This would not be possible without certain characterization tools that are used throughout the entire fabrication process.

3.4.1 Optical Microscope

An optical microscope is often used in between fabrication steps for a visual inspection, typical after development. Although the magnification and resolution are limited, it can discover defects or deviations in the resist after development. However, an optical microscope does not have the resolution to verify whether or not a waveguide structure's nanoscale features are within an acceptable range. Other characterization tools are required for such verification.

3.4.2 Scanning Electron Microscopy

A scanning electron microscope (SEM) is an imaging technique that uses a focused electron beam. It is a tool which is able to reach a magnification of 300000x [34]. The focused electron beam raster scans over the sample to achieve topographic images with a resolution of 1 nm. The theory behind the instrument that utilizes this technique is too detailed to include in this project, but some of the key aspects needs to be considered.

Figure 3.12 shows a typical setup of a SEM (other variations are possible). The electron source accelerates electrons towards the sample with energies between 1 keV to 30 keV [36]. From Figure 3.12, the beam travels through 1 anode, 2 condenser lenses and 1 objective lens. When going through the deflection coils (or scanning coils), where the beam is deflected and raster scanned over the sample. The objective lens focuses the beam, so that the beam that hits the sample has a diameter of less than 10 nm [37].

3.4.3 Interaction Volume

The different detectors are able to detect various signals being created as a result of electrons being scattered at the sample. Electrons from the beam are scattered from different depths in the sample, known as the interaction volume. When the beams is raster scanned over the sample, there are mainly two signals that are detected: *backscattered electrons* (BSE) and *secondary electrons* (SE). In Figure 3.13 the different depths various particles can be detected. Other particles like x-ray photons and Auger electrons are used for chemical analysis rather than topographic analysis, but are not used in this project.

SE are the result of inelastic collisions between the incident electrons from the beam and the atoms in the sample. Only those electrons that are formed in the first 2 nm from the surface escapes. The low energy, which is < 50 eV, allows the electrons to be detected as SE [37]. These electrons yields a topographical image with high contrast, and is the main imaging mode when collecting data in this project. The signal from the SE are gathered by applying a positive bias to the SE detector, which can be seen in Figure 3.12.

BSE are similar to SE, but are the result of elastic collisions directed back to the sample surface. These elastic collisions gives the BSE higher energy compared to SE, so that they are able to escape from further inside the sample. This can also be seen in Figure 3.13. However, this does reduce the resolution of the BSE signal imaging, but it also reveals more details of the sample since it penetrates deeper. Also the BSE are dependent on the atomic number, meaning that the BSE generated image also yields a elemental contrast image.

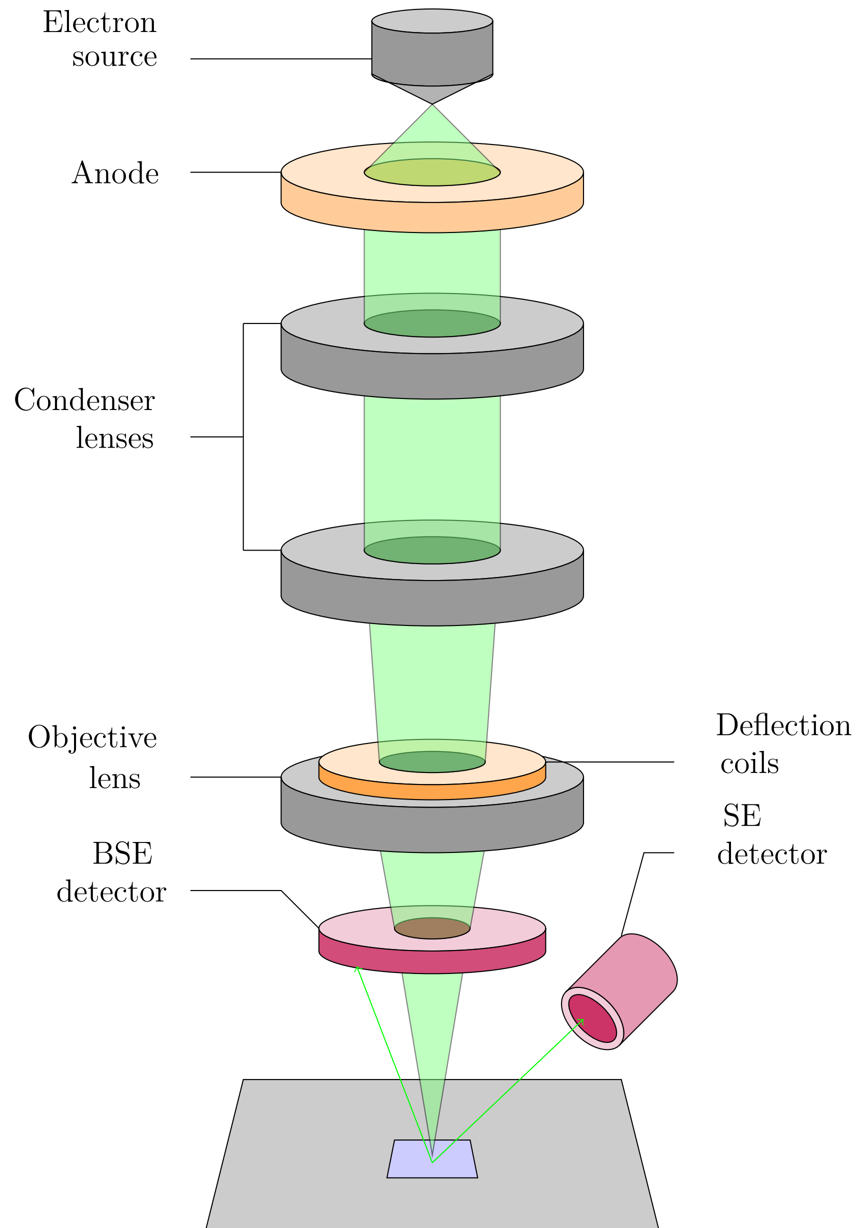

Figure 3.12: Schematic of a scanning electron microscope. The deflection coils are used to deflect the beam so the sample can be raster scanned. The two main detectors in a SEM is the BSE detector and the SE detector. Figure is adapted from [35].

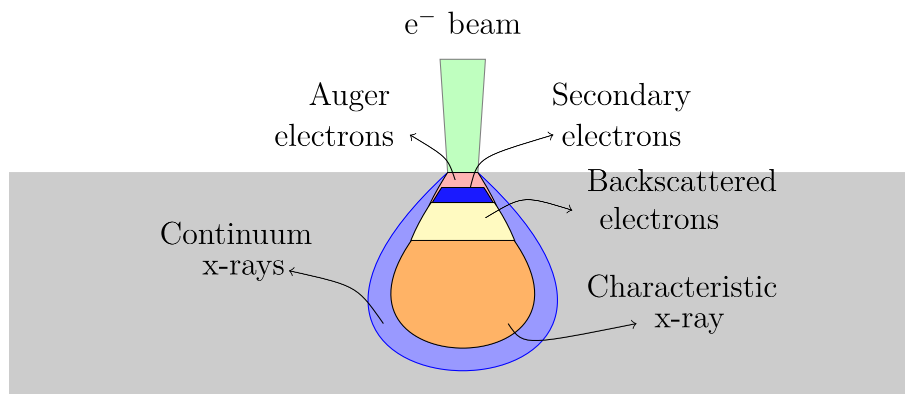

Figure 3.13: Interaction volume of where different particles escapes and can be detected. Figure adapted from [38]

4 | Experimental Procedure

A thorough account of the procedure used to optimize the MARC devices will be covered in this section. Prior to performing any laboratory work, a theoretical framework and simulations was performed to optimize values for the various parameters. The laboratory section includes both fabrication and characterization of the MARC sensor. In addition the routine for capturing and analyzing the output signal of the MARC sensor will be described.

Before showing the experimental method for the MARC devices, a few preliminary calculations were performed prior to the complete simulations of the MARC sensors, such as the *effective mode index analysis* and waveguide losses.

4.1 COMSOL simulations

COMSOL was extensively utilized to simulate the design of the MARC sensors. A bottom-up approach as used, where the different components of the MARC sensor were optimized separately in order to estimate the physical dimensions of the device

In order to fine tune the parameters, components such as the 3dB coupler at input/output, the add-drop ring resonators, and the Mach-Zehnder interferometer (MZI) were simulated to achieve optimal conditions. The design and optimization of these components are covered in Sections 4.1.4 - 4.1.6. Furthermore, each individual component was then put together to create a variety of MARC sensors with different angular separations. The MARC devices used in this thesis were constructed using three different angular separations, namely: 90°, 135°, and 240°. The main purpose of this optimization is to balance the two interferometer arms.

The balancing had to be done so that the phase between the two waveguide arms would not be out of phase (see Section 2.2). A phase difference between the two waveguide arms will cause noise in the transmitted signal, thus distorting the measured intensity.

Table 4.1: All refractive indices used during the simulations. All values except for a-Si in 2D are taken form [39], which is calculated in Section 4.1.3.

Material	Refractive index (n)
Air	1
a-Si in 2D	3.44784
a-Si in 3D	2.8332
SiO_2	1.4443

4.1.1 Physical Setup

During the entirety of the project the *Electromagnetic waves, frequency domain* were chosen as *Physics* together with *Wavelength domain* as the *Study*. Given that the real physical setup consist of a Thorlabs TLK-L1550M laser that spans from wavelengths 1500 nm to 1600 nm, the use of the wavelength domain study compared to the alternative Study *Frequency Domain* made intuitive sense. This module made it possible to enable calculation of propagating electromagnetic waves through the waveguide devices.

4.1.2 Parameters

During the modeling of the simulations, certain parameters were defined to simplify the geometry of the structures. Some of the parameters are of no particular importance, as they are coordinates to alleviate some tedious labor during the geometry building and will not be discussed. All the relevant parameters are presented in Table 4.2. In the aforementioned table there are parameters derived from Section 4.1.3.

Table 4.2: Different parameters used during the simulations in COMSOL.

Name	Value	Description
n_core	2.8332	Refractive index of the core (see Section 4.1.3).
n_cladding	1	Refractive index of cladding, i.e. air
k_core	2.5×10^{-5}	Real term of the refractive index of the core
k_cladding	0	Real term of the refrative index of the cladding
wg_width	500 nm	Waveguide width
cladding_width	3500 nm	Cladding width
bend_radius	14 nm	Bend radius of the waveguide
3dB_coupling	161.5 nm	Coupling distance in 3dB coupler
3dB_length	5.86 nm	Coupling length in 3dB coupler

Not all parameters represent their real physical value, but are rather estimated to a given value so that the simulations would yield optimized results. Hence the refractive index is tailored so that the simulations can be carried out in a two-dimensional

space (see Section 4.1.3). The coupling distance represents the distance for which the incoming light is split evenly in the simulation, and is therefore not representative of a real physical coupling distance. Such a coupling distance would have to be derived from theoretical calculations and experiments. The value of the coupling distance, 161.5 nm, was determined from the early simulations where a standard ring resonator of radius 30 µm was optimized.

4.1.3 Preliminary Simulations

Prior to conducting simulations for the individual components used to create the multiplexed MARC device, a set of preliminary simulations were carried out. This was done to find different parameters that was essential to create a more realistic simulation environment. The experiment and the following results will be presented together in Sections 4.1.3 due to practicalities.

Effective Mode Index Analysis

A calculation of the effective mode index was performed prior to the simulations of the MARC device. A SiO_2 layer of thickness 1 µm and a Si layer of thickness 220 nm with refractive index 1.4443 and 3.4784, respectively, were simulated in a three-dimensional space. A third and final layer was added on top, which consisted of air with refractive index of 1. The layout of these layers are shown in Figure 3.4. The mode analysis searched for one single mode around the value 3 (see Section 3.2.1 for why the value 3 was used), which yielded an effective refractive index of $n_{eff} = 2.8332$. This value is used throughout the entirety of the project.

Waveguide Losses

In a perfect waveguide there will be no losses during propagation, and it can in theory propagate infinitely without losing power. In order to make a closer approximation to a real physical device, some loss is added to the simulation. The waveguide was given an absorption coefficient by introducing an imaginary part to the refractive index, k_i. By sweeping over several values of k_i along a waveguide of a fixed length of 100 µm it was possible to determine the correct k_i. This value turned out to be $k_i = 2.5 \cdot 10^{-5}$.

Although an imaginary part of the refractive index alters the absorption losses in the waveguide, it was determined that it would not be used for the MARC devices since it only made the signal become weaker over time. A decision to leave

Bending Radius

An optimal bend radius had to be determined. Although the losses due to a waveguide bend is of importance, it is also desirable to have a bending radius in which the

device maintains its compactness. A waveguide with a 180° turn was created, and the transmission of light was recorded. A parametric sweep from 8 µm to 30 µm was carried out at a fixed wavelength of 1553 nm. The results show little to no loss due to the bending in the waveguide. Therefore a bend radius of 14 µm was chosen as the suitable bending radius - keeping the modelling structure compact.

4.1.4 3dB Coupler

The 3dB coupler is designed to split the incoming light equally into two waveguide arms. A coupling distance of 161.5 nm was used in the coupling region. Initially the experiment was going to use a wavelength sweep from 1500 nm to 1550 nm, and this interval was also used for the simulated beamsplitter which is why the 3dB coupler is simulated with the aforementioned wavelength interval. However, for the MARC simulations and laser measurements a new interval is used: $\lambda_0 \in [1522.5, 1547.5]$ nm. This is because the theoretical FSR_e is far away from 50 nm, thus the computational requirement is reduced by reducing the wavelength interval. The reason for using the specific wavelength interval is because the working wavelength range of a Thorlabs TLK-L1550M laser is 1500-1580 nm. However, a bandwidth of 50 nm was used to gain more information about this vital component.

In order to determine the optimal coupling length, L', a parametric sweep was performed on the coupling length. A perfect beamsplitter with a 50/50 distribution is hard to achieve over a wavelength interval of 10 nm, but the experiment still yielded an acceptable result with a maximum imbalance of a 53/47 distribution. The optimal coupling length was *L*' = 5.86 µm. The reason for the imbalance is the wavelength-dependent coupling [40].

4.1.5 Ring Resonators

Each of the three rings resonators that are used in the multiplexed MARC device had to be optimized. Firstly the coupling distance between the bus waveguide and ring resonator had to be found, which was different for all ring resonators due to different ring radii. For each ring resonator the key parameters were optimized to achieve extinction during resonance. The full-width half-maximum (FWHM) also had to be narrow enough at the resonance dips, so that the multiplexed signal would not overlap with other resonance peaks. When the coupling distance is set so that critical coupling occurs, the different parameters of the ring resonator can be derived. Specifically, these are the FWHM and the Q-factor.

4.1.6 Mach-Zehnder Interferometer

The Mach-Zehnder interferometer (MZI) had to be simulated as well. As the MARC sensor is constructed upon the MZI, it is critical to achieve an optimized

interferometer, as well as gaining useful insight into how the MZI behaves. . With the now optimized 3dB coupler as both input and output of the MZI, a transmission study of the output signal was conducted for the interval $\lambda_0 \in [1500, 1560]$ nm. The two waveguide arms were of identical length, so that the phase difference would be zero.

4.1.7 MARC Sensors

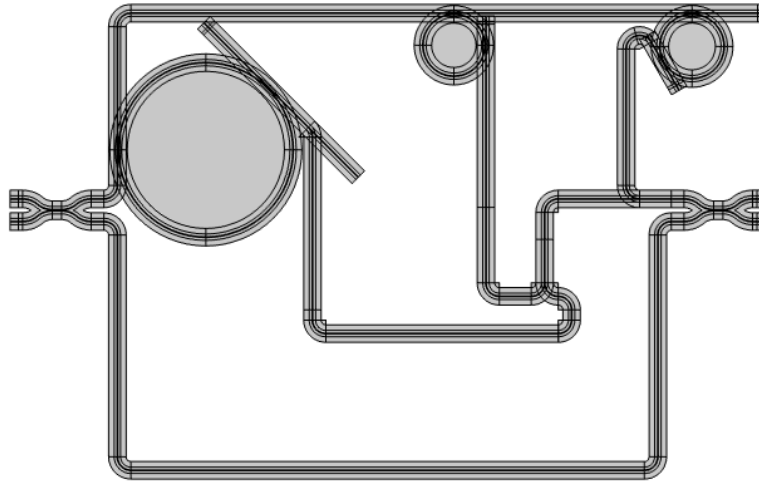

Figure 4.1: Multiplexed MARC device in COMSOL with MARC90, MARC135, and MARC240 contributing to the output signal.

The MARC senors of angular separation 135°, 90°, and 240° were all designed inside the same MZI in a so-called multiplexed configuration. This was done so that the individual signals from each of the MARC sensors could be composited into a single signal. The geometry of the multiplexed MARC device consisting of the ring resonators is shown in Figure 4.1. Each of the three MARC sensors will henceforth be referred to as MARC90, MARC135, and MARC240, based on their angular separation.

The three different angular separations were determined based on the theoretical transmission spectrum of the individual, so that the resonant peaks would not overlap, and are shown in Figure 5.7.

In order to make the device balanced, the rightmost MARC device, MARC240, was created first. To balance it, the length of the lower waveguide arm was tweaked, so that the phase difference would be approximately equal to zero. Once the MARC240 yielded a balanced and readable signal, the next MARC sensor can be introduced into the signal as well.

The MARC90 also needs to be balanced in relation to the balancing arm. Since the

length of the latter arm is directly responsible for the signal in the MARC240, the waveguide arm of the MARC90 has to be adjusted for proper balancing. Lastly the MARC135 was balanced in a similar manner as the MARC90, where the waveguide arm was adjusted.

4.2 Fabrication and Characterization

Figure 4.2 summarizes the fabrication process for creating a SOI photonic MARC waveguide sensor. This figure shows the most important steps, which will all be elaborated on in Sections 4.2.1-4.2.4. Different characterization tools are also used throughout the fabrication, but it is the SEM that is most important and will be elaborated on in Section **??**. The various steps that are included in the fabrication will be covered chronologically to make it more comprehensible.

The fabrication process is similar to the process used by Yadav et al. in [3]. The fabrication process starts with depositing a 220 nm thin film layer of a-Si on a SiO_2 4" wafer using PECVD. A thin layer of e-beam resist is spin coated onto the wafer, where the pattern of the MARC sensor is written into the resist using EBL. The resist is developed, so that ICP-RIE can be used to etch through the patterned a-Si layer. Following the etch, the resist is removed and the sample is cleaned. Finally a new thin film of photoresist is spin coated onto the wafer to create inverted tapered waveguides at the input- and output ends of the MARC sensor.

4.2.1 Thin Film

The fabrication process starts with a 4" silicon wafer, which has a top layer of SiO_2 with a thickness of 1 μm, deposited thermally. This process is beneficial to waveguide operations, as it keeps the surface roughness from the silicon wafer [41].

The PECVD instrument is an Oxford Instruments Plasmalab System 100, and was used to deposit a thin film of a-Si of thickness $\approx$ 220 nm onto the wafer. The different steps involved in the deposition is elaborated in the following list.

Cleaning: The 4" silicon wafer is cleaned in an ultrasonic bath of acetone in 5 minutes, before it is rinsed with IPA and dried with a N_2 gun.

Pre-conditioning chamber: To avoid contamination from the previous PECVD operation with a different PECVD chemistry, a short deposition of 5 minutes is performed on a dummy wafer. This is done with the intended recipe so that the chamber is stabilized [42].

Deposition: The a-Si thin film is deposited using a recipe with the parameters from Table 4.3. Both silane (SiH_4) and argon (Ar) were used to create the PECVD chemical environment.

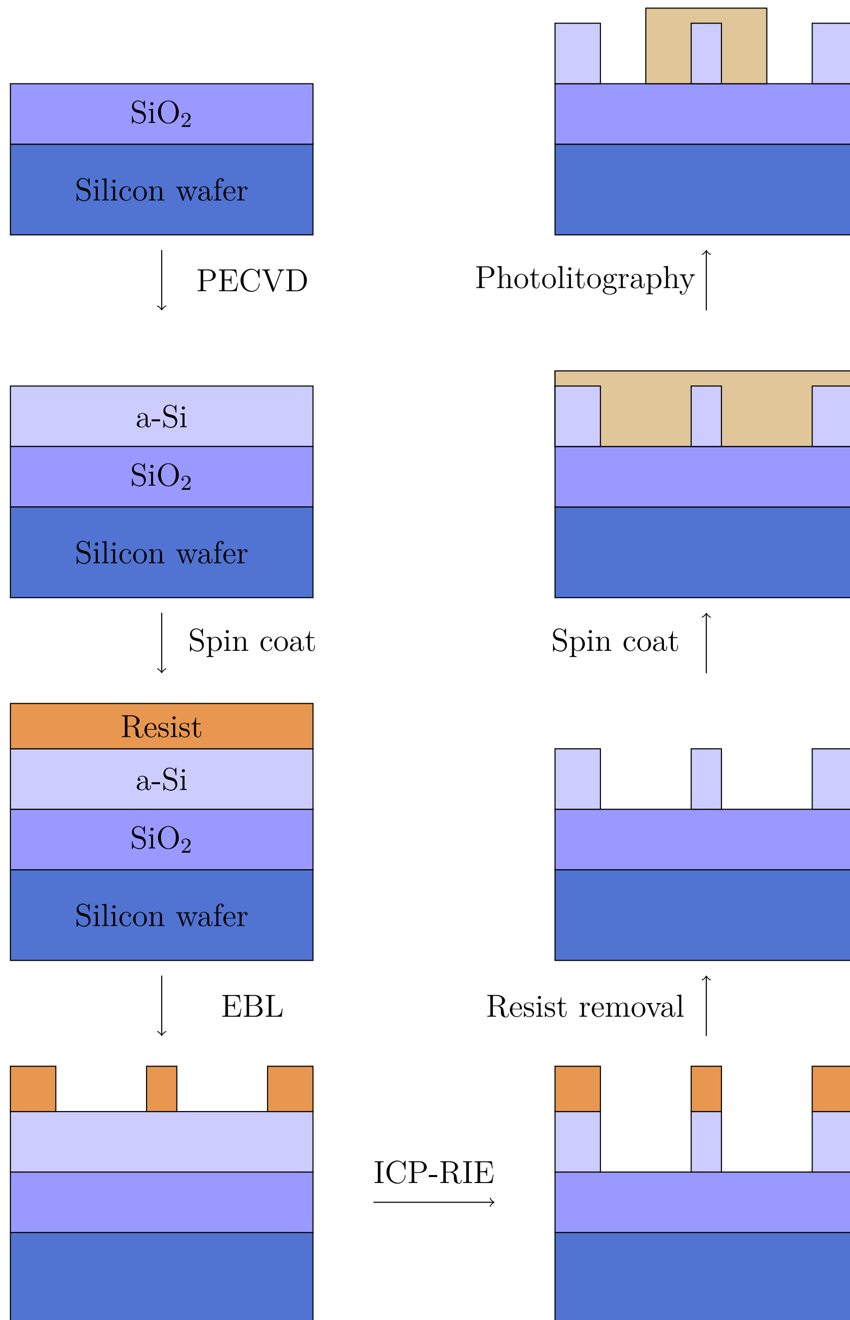

Figure 4.2: Schematic flow-chart of the cross-sections showing the processing steps in the fabrication of the MARC sensor. The thicknesses and widths are not to scale.

Table 4.3: PECVD parameters used for growing a a-Si thin film on a 4" silicon wafer.

Parameters	a-Si
SiH_4	50 sccm
Ar	150 sccm
LF power	200 W
Pressure	500 mTorr
Temperatur	300 °C
Growth time	3 min

Thickness verification: A reflectometer is used to verify that the thickness of the a-Si thin film is correct.

Thickness verification

The thin film of a-Si with a approximate thickness of $\approx$ 220 nm was measured using a reflectometer - more specific the Filmetrics F20 Tabletop Film Thickness Measurement System. Both the materials used and the thickness of the thin film are within the restrictions of the reflectometer [43].

The instrument is calibrated to be able to measure the thickness of the film, and is done in a 3 step process by measuring a reference silicon wafer, the wafer with the thin film, and the background of the reflectometer. To ensure that the thickness is correct, several thicknesses are measured at various locations on the wafer. Furthermore, the cross-section of the wafer was placed in a SEM to measure the thickness of the thin film. This was done to make sure the accuracy of the reflectometer was within an acceptable range.

4.2.2 Mask Pattern

The wafer is patterned so that is can be etched later in the fabrication process. Using EBL with an Elionix ELS-G100 100 kV EBL system at Nanolab, the e-beam resist is exposed to an electron beam that imprints the mask pattern. The workflow used is described in the following list.

Scribing: After the thin film deposition, the 4" wafer was cut into rectangular wafer chips of dimensions 20 mm x 25 mm. The scribing was done with a Süss MA-100 manual wafer scriber, ensuring that the 4" wafer is cut into identical chips along the crystal axis of the material. To break the sample a set of wafer cleaving pliers were used.

Cleaning: The wafer is cleaned using acetone in a sonic bath for 2 minutes, mainly to remove residue from the scribing step. It is then rinsed with IPA and dried with a N_2 gun.

Table 4.4: Spin coat parameters used for spin coating a thin film of e-beam resist with a 220 nm thickness.

Step	Time [s]	Speed [rpm]	Acceleration [rpm/s]
1	7	1000	500
2	60	8000	800

Table 4.5: The parameters used for the EBL to ensure that the pattern is created optimally.

Parameter	Value
Acceleration voltage	100kV
Beam current	2 nA
Aperture	120 μm
Beam diameter	2.3 nm
Write field	500 μm
Dots	1000000
Area dose	130 μC/cm^2
Dose time	μs/dot
Feed/Scan pitch	8 nm/8 nm

Spin coating: The e-beam resist Allresist AR-P 6200 (CSAR 62) is spin coated on the wafer chip. The parameters can be seen in Table 4.4, which yields a film thickness of ≈ 220 nm.

Soft bake: The wafer chip is then baked on a hotplate at 150 °C for 1 min, so that the solvent from the e-beam resist is evaporated.

Exposure: The parameters for the EBL exposure can be seen in Table 4.5. Although it is possible to use beam currents as low as 100 pA, it was not necessary in this project as there is no demand for such a high resolution. A beam current of 2 nA was used instead.

Development: The wafer chip is developed by immersion in a beaker of Allresist AR 600-549 developer for 1 min. Then the wafer chip is moved to a beaker with IPA where it is agitated to remove any leftover developer, before it is again moved to a new beaker with IPA. Finally the sample is dried with a N_2 gun.

Plasma cleaning: To remove any excess photoresist the wafer chip is placed in the plasma cleaner for 1 minute at 50/50 O_2 flow/power is used.

Optical microscope: An optical microscope with 100x magnification is used to control the quality of the development. If there are defects on the wafer chip, the resist is removed and a new attempt at spin coating is performed.

Table 4.6: Parameters used for etching of the 220 nm a-Si layer.

Parameters	Value
CHF_3	7.5 sccm
SF_6	50 sccm
Pressure	15 mTorr
Temperature	20 °C
Time	40 s

4.2.3 Etch

The etch on the 220 nm thick layer of a-Si is etched in an Oxford Plasmalab System 100 ICP-RIE 180 at Nanolab.

Pre-conditioning chamber: Similar to the step done with the PECVD instrument, a short deposition on a 4" dummy wafer is performed to avoid contamination and to "calibrate" the chamber.

Fomblin oil: To ensure that the wafer chip is secured on the 4" carrier wafer, a thin layer of Fomblin oil is used as glue. This also provides better heat conduction, and is especially important as the sample holder is temperature regulated during the etching process.

Etching: The wafer chip is etched with the parameters presented in Table 4.6. This ensures that the wafer is etched anisotropically, as illustrated in Figure 3.11.

Resist removal: The CSAR 62 e-beam resist is removed using AR 600-71. This is done by sonication for 5 minutes. The sample is then rinsed with IPA and dried with a N_2 gun.

4.2.4 Inverted Tapers

Inverted tapered waveguides are fabricated to increase the coupling efficiency when coupling light between the lensed fiber and the waveguide input/output. The polymer waveguides are made using Omnicoat and MicroChem SU-8 photoresist [44]. To ensure the desired thickness of MicroChem SU-8 is achieved, a specific blend is made called SU-8 2000 (SU-8). The sample is exposed in a Heidelberg MLA100 maskless aligner (MLA), and then being developed in a Micro Resist Technology mr-Dev 600.

Plasma cleaning: The sample is cleaned in a plasma cleaner for 5 minutes with 50/50 O_2 flow/power. This is to remove any resist that is left on the etched sample [45].

Spin coating: There are two layers spin coated onto the wafer. The first layer is

Table 4.7: The parameters used to spin coat a layer Omnicoat and a layer of SU-8.

Step	Time [s]	Speed [rpm]	Acceleration [rpm/s]
1	10	1000	500
2	50	4000	1000

a Omnicoat, which is a thin layer that improves adhesion between the silicon surface and the SU-8 photoresist [46]. SU-8 is then spin coated on top of the Omnicoat film. The parameters used for spin coating are presented in Table 4.7. This results in a SU-8 film thickness of 2 μm [44].

Soft bake: To ensure that the solvents are evaporated in a controlled manner, a two step baking process is used [47]. The first step is to bake at an initial temperature of 65 °C for 1 minute. The second step is to bake for 2 minutes at 95 °C. To avoid a quenching effect of the Omnicoat and SU-8 layer, the wafer is cooled down slowly without the use of a cold-plate.

Exposure: The wafer chip is placed in the MLA where it is aligned properly with the use of alignment marks. The parameters used for the MLA exposure are a dose of 1400 mJ/cm^2 with a 375 nm wavelength.

Post-exposure bake: This step is done to harden the SU-8. The heat treatment cross-links the exposed regions of the resist. The same procedure used for the soft bake is used in this step.

Development: The wafer chip is immersed in mr-Dev 600 for 1 minute and then rinsed in fresh developer to remove any photoresist that can contaminate the sample. It is then rinsed in IPA. The use of a N_2 gun can destroy the waveguide structure due to bad adhesion, so the sample is simply air dried.

Plasma cleaning: To ensure that there are no excess photoresist on the sample, a plasma clean of 50/50 O_2 flow/power for 1 minute is done.

4.2.5 Scribing and Breaking

A Dynatex DX-III scriber and breaker at Nanolab is used to scribe and break the sample. This instrument is very precise, and makes it possible to scribe off small parts of the wafer along the {100}-planes of the wafer. Since scribing leaves dust from the diamond tip carving into the sample, the sample is only scribed close to the edge, as oppose to scribing across the entire waveguide structure. This is done in "edge-scribe mode", and if the scribed line is parallel to the crystal axis it should leave a clean break. This step is important to give a clean input/output at the waveguide structures, so that the light is not scattered in different directions when coupling.

4.2.6 SEM

The FEI Aperon SEM was used for imagery during the fabrication process to verify and investigate the MARC sensors. Images were taken using both SE and BSE electrons for signal processing.

4.3 Transmission Spectrum Setup

A schematic setup of the devices used to measure the transmission response of the MARC sensor can be seen in Figure **??**. A Thorlabs TLK-L155M tunable laser is used as the input to a single-mode fiber with a lensed fiber tip. A Elliot three-axis XYZ stage is used to mount the fiber lens, where the stage can be adjusted in all three axes of movement. From the stage the laser from the fiber lens is focused onto the input of the MARC sensor. At the output of the MARC sensor, the output laser light is focused into a cleaved fiber, which is also mounted to an identical Elliot three-axis XYZ stage. The fiber is connected to a Thorlabs DET10C2 detector, where the signal is amplified Thorlabs PDA200C photodiode amplifier. The signal is connected to a National Instruments PCI-6024E DAQ. On the computer in the lab, a program called LabView[1] from National Instruments is used to control the lab setup. A custom made program in LabView was used control the wavelength sweeps of the laser, and was used by Yadav et al. [3]. The data obtained was stored in files, containing the data from the measurements.

[1]www.ni.com/en-no/shop/labview.html

5 | Results and Discussion

5.1 Individual Components

5.1.1 3dB Coupler

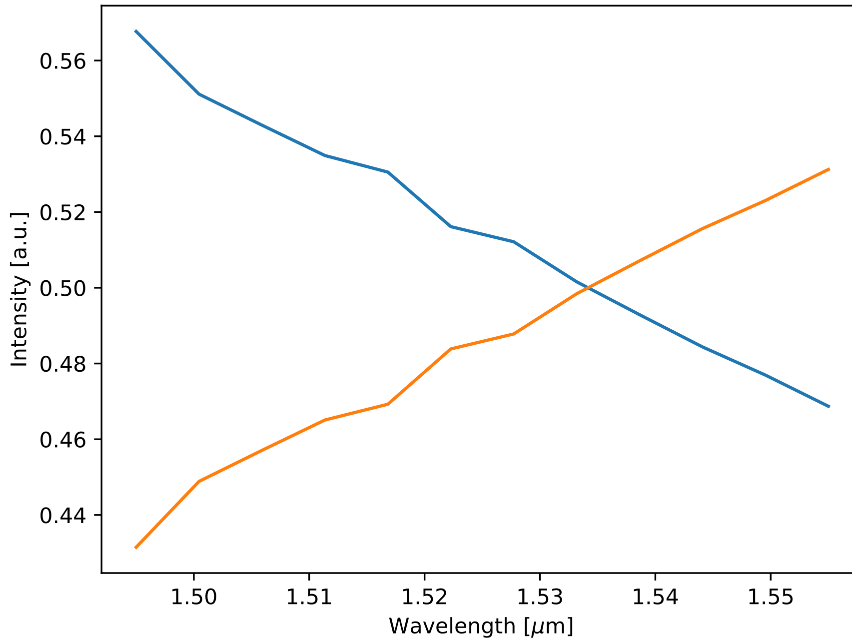

Figure 5.1: The linearity of the intensity spectrum of the 3dB coupler with respect to the wavelength. No losses due to absorption are accounted for in this model.

The 3dB coupler is designed to split the incoming light into two arms, as shown in Figure 5.2. This was done with a coupling separation of 161.5 nm, which was determined from the critical coupling of a ring resonator used early in the project. It is an arbitrary number, but it does result in coupling between the two waveguides. The coupling length, L' = 5.87 μm, which is the area where coupling occurs, is the distance that determine how much light is coupled. The simulations of the transmission spectrum were carried out in the wavelength interval $\lambda_0 \in [1500, 1560]$

nm, and is based on the interval of the Thorlabs TLK-L155M explained in Section 4.3. The splitting is not 50/50 throughout the entire interval, but a perfect splitting is achieved at around 1535 nm. The transmission spectrum for the 3dB coupler can be seen in Figure 5.1. At the two endpoints of the interval, the splitting is more imbalanced at 55/45 and 45/55 for 1500 nm and 1555 nm, respectively.

The uneven splitting does seem to manifest itself in the preceding simulations in the form of both periodic absorption peaks and ripples. There are designs that could improve the splitting ratio of the 3dB coupler[48][49], but due to time restrictions it was not realised. Also, the uneven splitting was first considered a problem after all the MARC simulations were carried out. Perfect splitting is hard to achieve, but the imbalance can be reduced by shortening the interval. Therefore the interval used for the simulations was $\lambda_0 \in [1522.5, 1547.5]$ nm.

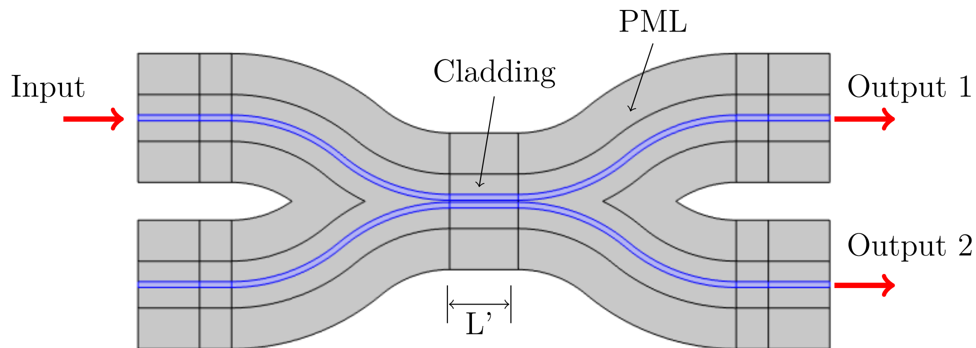

Figure 5.2: COMSOL model of 3dB coupler. The blue highlighted area is the waveguide, with the outer layers being the cladding and the PML. The input is split at the coupling region of the 3dB coupler, dividing the intensity between output 1 and output 2.

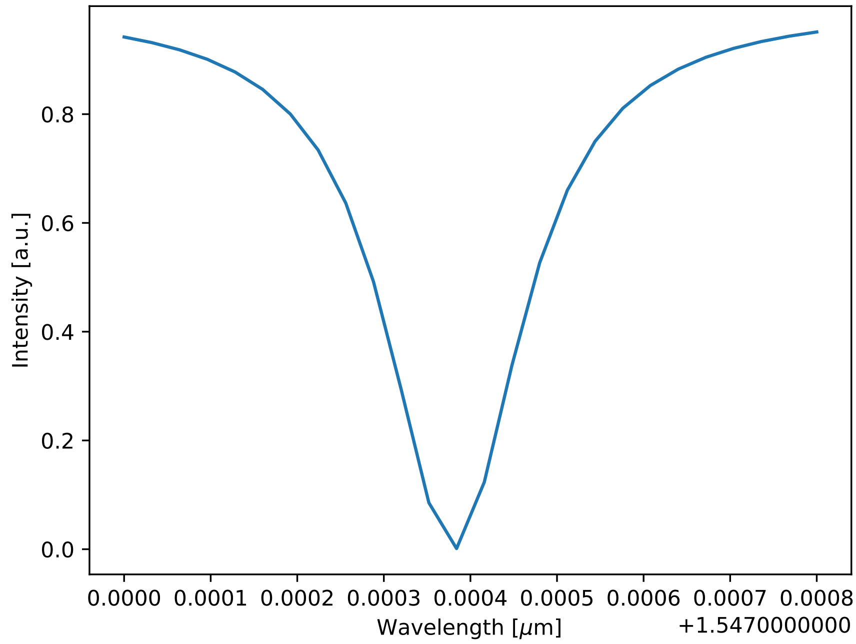

Figure 5.3: Transmission spectrum of 20 μm radius add-drop ring resonator at critical coupling.

5.1.2 Ring Resonators

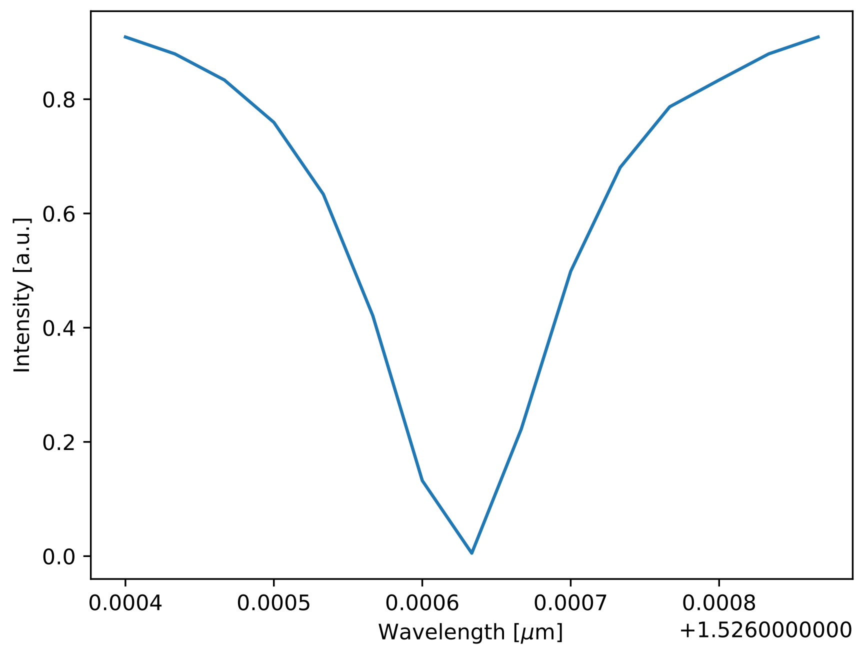

Figure 5.4: Transmission spectrum of 25 μm radius add-drop ring resonator at critical coupling.

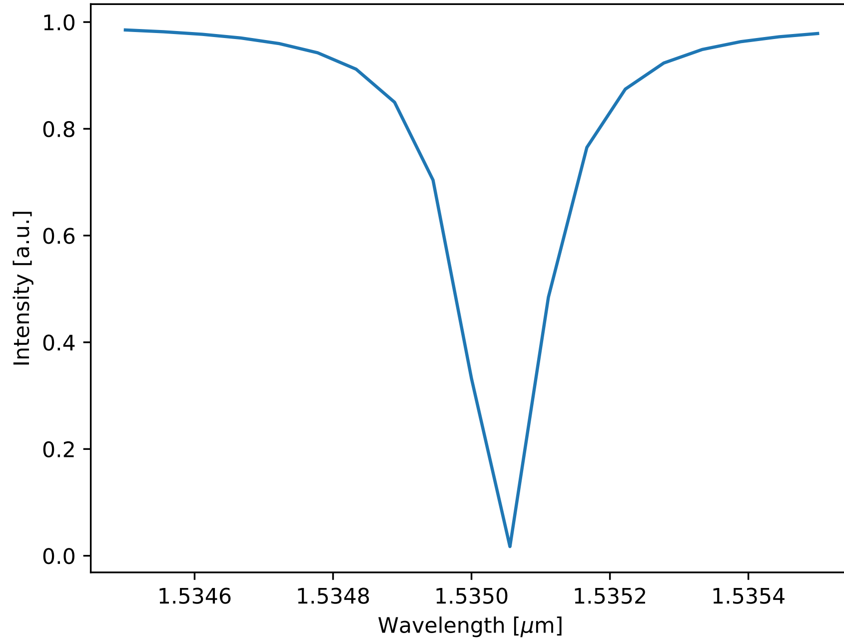

Figure 5.5: Transmission spectrum of 55 μm radius add-drop ring resonator at critical coupling.

Each of the three ring resonators used in the multiplexed MARC device was simulated individually. By carefully tweaking the coupling distance, the point(s) at which critical coupling occurs was found with its respective coupling distance. The critical coupling distance of each individual ring resonator together with the FWHM and Q-factor are presented in Table 5.1.

Table 5.1: Optimized coupling distance for each individual ring resonator with radii 20 μm, 25 μm, and 50μ to achieve critical coupling. No losses due to absorption was accounted for in the simulations.

Ring Resonator	Ring Radius	Coupling Distance	FWHM	Q-factor
240°	20 μm	178.3 nm	0.190 nm	$\approx$ 8100
90°	25 μm	183 nm	0.145 nm	$\approx$ 10600
135°	55 μm	192 nm	0.120 nm	$\approx$ 12700

Each of the ring resonators shows critical coupling, where the intensity is essentially extinct and with narrow FWHM values. The Q-factor was determined using Equation 2.42, and are calculated using FSR and FWHM. The reason for the differences in Q-factor, is mainly due to the difference in ring radius. First of all, when the radius increases, there is also less loss due to the bending radius of the ring. Secondly, there is also an increase in optical path inside of the ring [50]. This means that more optical power is stored inside the ring resonator, compared to the losses that occurs inside the ring due to scattering and absorption. Finally, the modal volume

also decreases as a result of an increase in ring radius. This corresponds to a higher Q-factor [51].

5.1.3 Mach-Zehnder Interferometer

An individual MZI was simulated with identical arms in COMSOL and is shown in Figure 3.3d). The transmission spectrum of the stand-alone structure is shown in Figure 5.6.

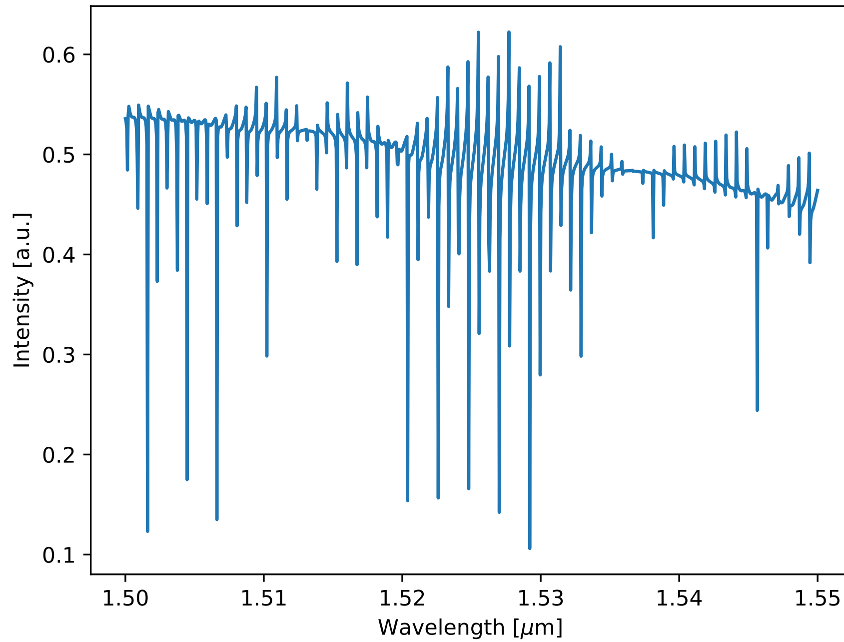

Figure 5.6: Simulated Marc-Zehnder transmission spectrum for a stand alone MZI. Notice the periodic absorption peaks and the ripples that oocure throughout the sepctrum.

The signal in Figure 5.6 is very noisy, which can be seen from the ripples that occur throughout the transmission spectrum. Although there is a non-uniformity in the absorption spectrum, there is also a pattern that can be seen in the spacing between the absorption peaks, i.e. the collection of ripples seen in the intervals [1501,1510], [1520,1533], and [1539,1550]. Ideally the signal should have been more uniform, and the reason for the non-uniformity of the signal is not clear.

The main problem might be the non-uniform 3dB coupler (see Figure 5.1) where the splitting is 50/50 at around 1535 nm. From the MZI transmission spectrum the signal becomes less varying after reaching 1535 nm. This does indicate that the non-ideal 3dB coupler is one of the reasons for the unwanted peaks in the signal.

The ripples seem to be present throughout the entire signal with varying intensity. This means that the problem is most likely not due to the uneven splitting of the

3dB coupler. Another plausible reason could be that the entire MZI structure is acting like a Fabry-Perot interferometer, which occurs when light is reflected back and forth at the input and output ports (see Section 2.4.1. The FSR_λ is found from measuring the distance between two adjacent peaks in Figure 5.6, and was measured to be $\text{FSR}_\lambda = 0.76$ nm. By using Equation 2.30 the distance d is calculated to be ≈ 600 μm (by simply measuring the distance between input and output port in the simulation geometry). This mirror separation is fairly close to the length of the MZI, which is ≈ 480 μm. This length includes the distance from input port to output port. The fact that the calculated distance is close to being the same as the actual distance, this does implicate that the entire device acts like a Fabry-Perot cavity.

The ripples present in the signal will continue to affect the results in the forthcoming sections. As discussed in Section 5.1.1, there are possibilities to even out the power splitting in the 3dB coupler, and this could make the signal more coherent. This could alleviate the amplitude of the ripples, making the signal more readable by reducing the noise.

5.2 MARC Simulations

After the preliminary individual components were designed and optimized, simulations on the individual MARC devices were carried out in the following order; MARC240, MARC90, and MARC135. At this point the phase imbalances from coupling in the 3dB coupler and between the bus waveguide and ring resonators were accounted for by increasing the length of the arms. However, an attempt to balance the device turned out to be very tedious. Several simulations was conducted, with incremental changes to the balance arm in order to fine-tune the device. This had to be done for all three different MARC devices. The fine-tuning of the MARC135 sensor is shown in Figure **??**, where the length of the balancing arm is adjusted.

The transmission spectrum from each individual MARC sensor will be presented in Sections 5.2.1-5.2.3, as well as the parameters FSR, FSR_e, and Q-factor. The simulated MARC devices' geometrical configuration in COMSOL is shown in Figures 3.3a)-c).

5.2.1 MARC240

In Figure 5.8 the transmission spectrum of the intensity is shown for the MARC240 device. From the intensity spectrum it is clear that there are ripples throughout the wavelength sweep, similar to that of the MZI in Section 5.1.3.

If the ripples are disregarded, the signal is very symmetrical and does show Fano-like lineshapes at 1528 nm and 1541 nm. The peaks are narrow and easily recognizable, so that it can be distinguished in a multiplexed signal. The FSR and FSR_e are 7

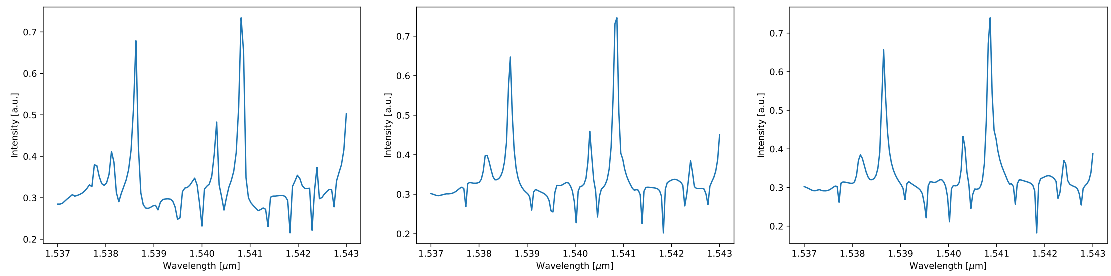

(a) 2.30 μm increase in balance arm. (b) 2.35 μm increase in balance arm. (c) 2.38 μm increase in balance arm.

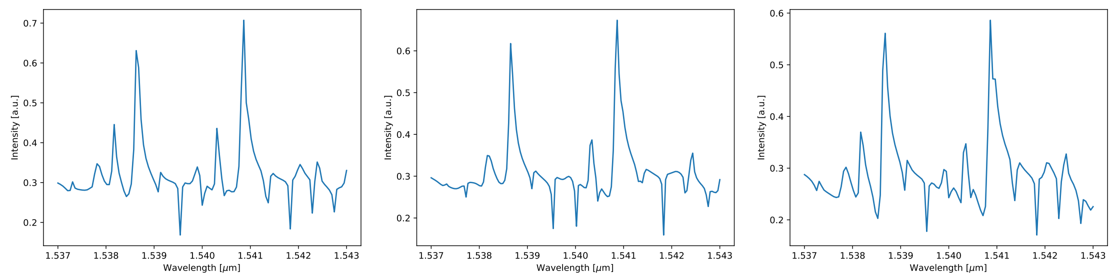

(d) 2.40 μm increase in balance arm. (e) 2.42 μm increase in balance arm. (f) 2.45 μm increase in balance arm.

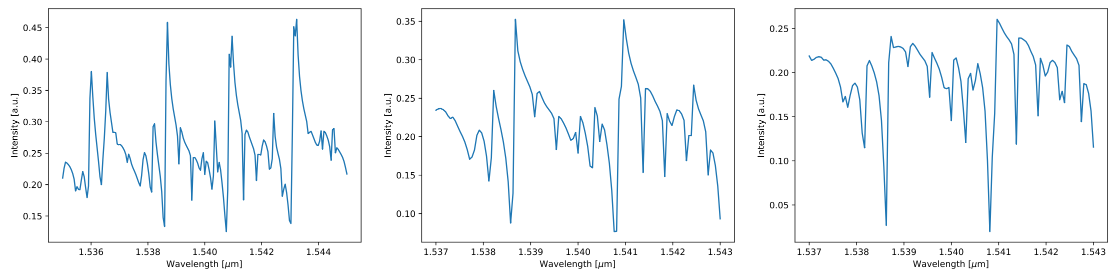

(g) 2.50 μm increase in balance arm. (h) 2.55 μm increase in balance arm. (i) 2.60 μm increase in balance arm.

Figure 5.7: The transmission spectrum for the MARC240, where a small wavelength interval was used to investigate which balance arm length would yield a balanced MARC device.

nm and 15 nm, respectively. By looking at the broadness of the peaks, the quality factor Q ≈ 6400. Compared to the quality factor of the 20 μm ring resonator in Figure 5.3, which was Q ≈ 8100 (see Table 5.1), it is very close to the aforementioned value.

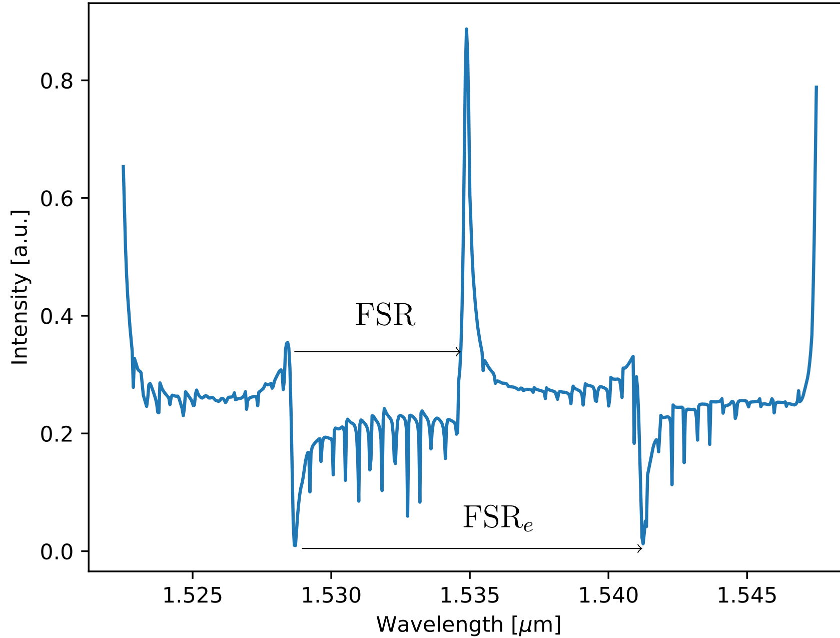

Figure 5.8: Transmission spectrum of the simulated MARC240 device. The amount of ripples are acceptable, but increases around the 1530 nm point. FSR_e = 18.5 nm and FSR = 9.25 nm.

5.2.2 MARC90

The transmission spectrum of the MARC90 device is shown in Figure 5.9. Due to the high FSR_e, the simulation had to be repeated for a larger wavelength interval (1500 nm to 1550 nm). The Fabry-Perot ripples are present throughout the spectrum, but does seem to be most apparent around 1530 nm. This is very similar to how the ripples behave in the MARC240 (see Figure 5.8). However, the ripples do have a stronger amplitude, which might have to do with the imbalance of the device.

Less time was used to balance the MARC90 device due to time restrictions, which could be the key reason for the ripples. Another reason is the difference in the geometry. More curves could potentially distort the Fabry-Perot resonance, and thus result in more ripples.

Although the ripples are present, the signal is still readable. At 1515.5 nm there is a close-to symmetrical Lorentzian lineshape, which seems to followed up by two peaks on each side. Although the signal is very distorted, it is possible to measure some important parameters.

The FSR_e and FSR are measured to be 25.6 nm and 6.5 nm, respectively. The Q-factor is measured to be Q ≈ 7800, while the Q-factor for the ring resonator is Q ≈ 12700. The difference between the two measurements are greater than that of the MARC240. This could be because of the curvatures in the geometry. With more curves, there is a possibility that the peaks are broadened due to absorption in the geometry. Another plausible reason is that phase is out-of-balance, so much that the Lorentzian shapes will have broader peaks and lower roll-off.

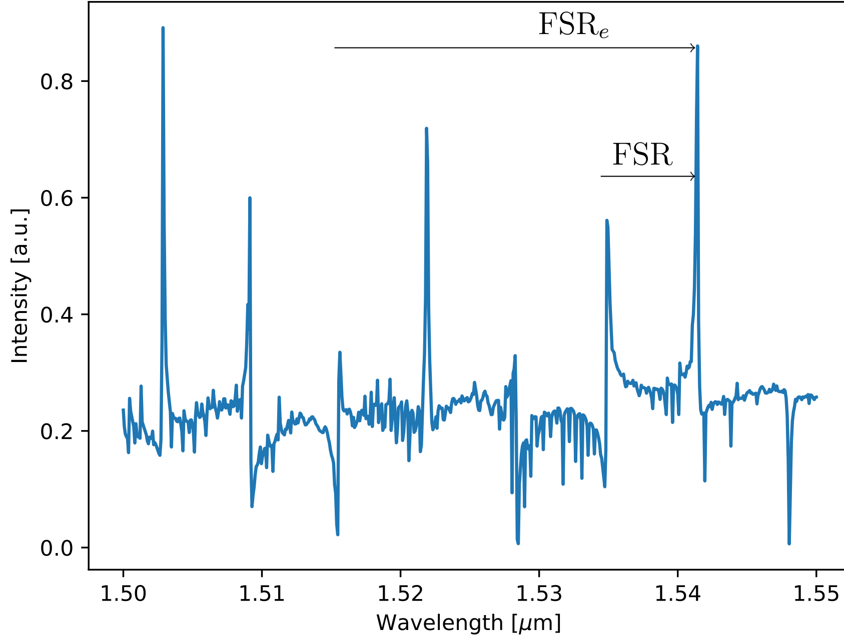

Figure 5.9: Transmission spectrum of the simulated MARC90 device. The amount of ripples are present throughout the spectrum, but increases around the 1520nm - 1535 nm. FSR_e = 25.6 nm.

5.2.3 MARC135

The transmission spectrum of the MARC135 is shown in Figure 5.10. The signal is highly distorted with ripples along the whole spectrum. Compared to the signal of the MARC90 and MARC240 (see Figures 5.9 and 5.8) the ripples have a higher spacing, making it harder to interpret the signal.

When comparing the result to the theoretical transmission spectrum in Figure 2.8, it is clear that signal is not too far away of what it should be. The FSR of the theoretical MARC135 is ≈ 2.0 nm, while the FSR of the simulated MARC135 is ≈ 2.5 nm. When it comes to the symmetries of the simulated signal, it is difficult to find any similar peaks, i.e. the peaks are very similar. At 1534 nm and 1536 nm there are two peaks closer to each other compared to other places in the transmission spectrum. Since the FSR_e of the theoretical spectrum in Figure 5.10 is ≈ 15 nm, the

peaks are most likely at the edges of the wavelength interval (or slightly outside of the interval). If the signal was more balanced the signal could be readable. Looking at the quality factor, it turn out that it is ≈ 2500.

This results is far from promising and the MARC135 structure should have been balanced more. An attempt was made, but an similar approach was successfully used for the MARC240 and MARC90 without much problems.

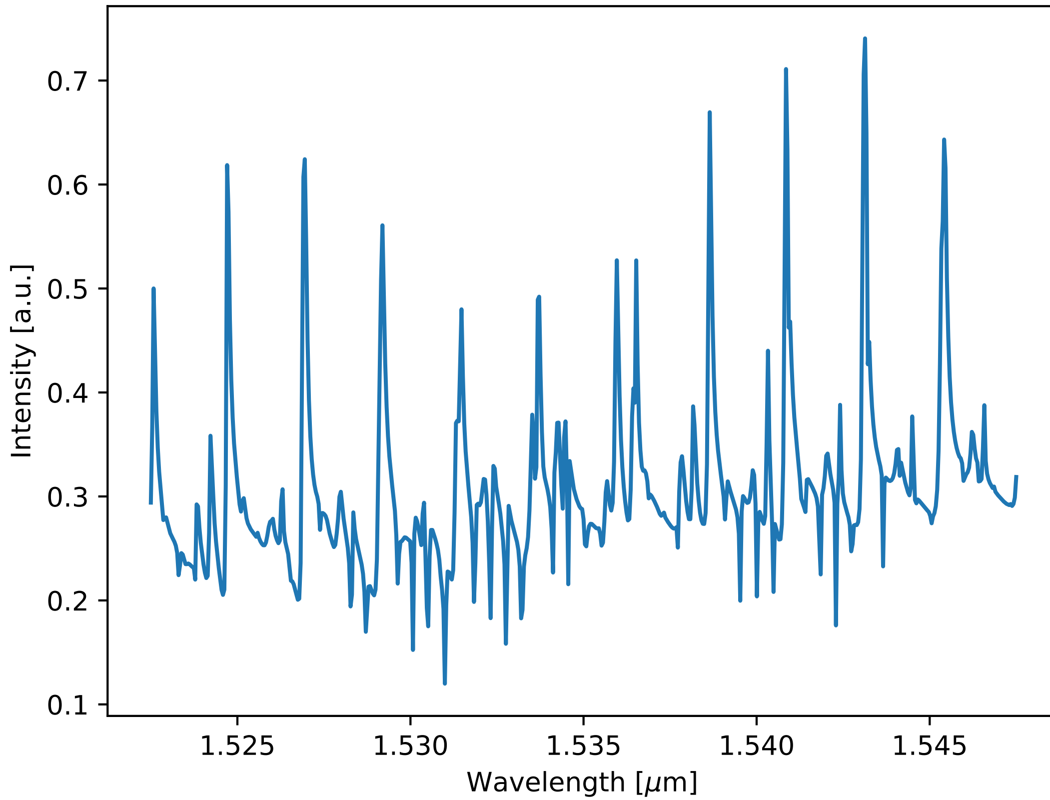

Figure 5.10: Transmission spectrum of the simulated MARC90 device. The amount of ripples are present throughout the spectrum, but increases around the 1520nm - 1535 nm. $FSR_e = 25.6$ nm.

5.2.4 Multiplexed MARC

The transmission spectrum of the multiplexed MARC is shown in Figure 5.11. Keeping in mind that the MARC135 was not properly balanced, it is to be expected that the multiplexed signal is affected by this. Since the MARC240 have a high FSR compared to the other MARC sensors, it does not really affect the signal all that much. Therefore the presence of the resonant peaks in the MARC135 is quite clear.

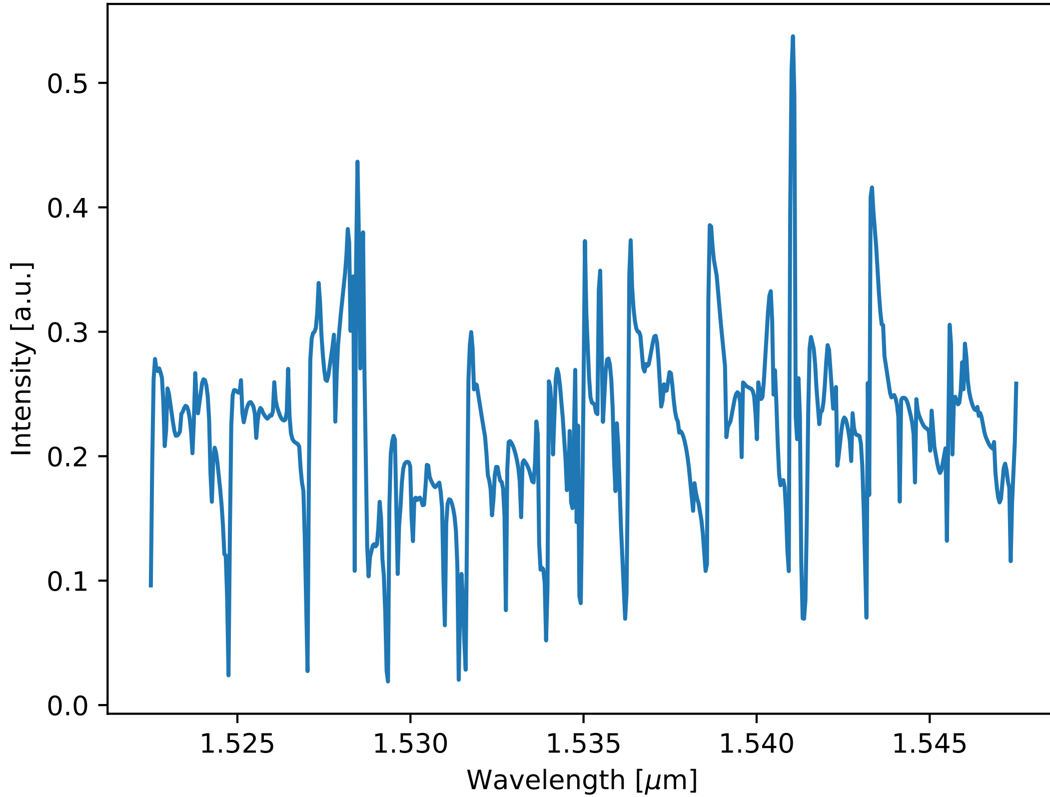

Figure 5.11: Transmission spectrum of the multiplexed MARC device.

5.2.5 Fabrication Results

Several wafer chips were fabricated in the lab, but only one wafer chip was successfully fabricated and tested. The process of trail and error to optimize the fabrication steps were tedious. Certain faults would render the wafer chip useless, and the fabrication process had to start from the beginning.

The last wafer chip, which is also the one tested in Section 5.2.6, did make it through the entire fabrication process. This was done with the step-by-step process explained in Section 4.2. However, at the end of the fabrication the chip had to be scribed, which was not done properly and resulted in poorly made input and output ports. The result of the poor scribing can be seen in Figure 5.12. Here the white area that borders with the dark area on the left-hand side is not a straight edge. This means that there is a high chance of the output being scattered in different directions when exiting the waveguide. The results from the tested chip will be presented in Section 5.2.6.

The wafer chip was created with 20 individual MARC sensors: 5 identical MARC240, 5 identical MARC90, 5 identical MARC135, and 5 identical multiplexed MARC with

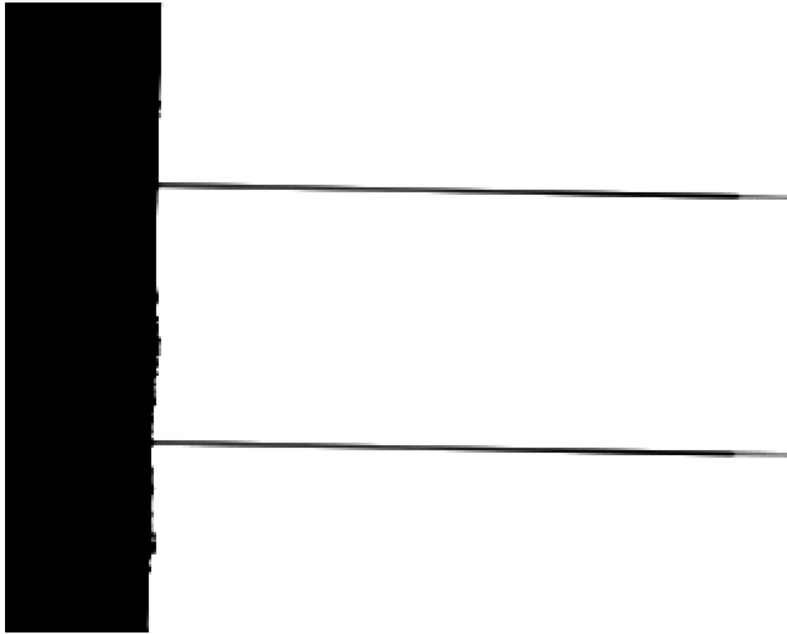

Figure 5.12: An image take with an optical microscope, showing the two output ports of the MARC sensor. The white area is the wafer chip and the black lines are the waveguides. The edge of the MARC sensor is not straight, meaning that the output light will be scattered. The area where the black line becomes thicker is the start of the inverted tapers.

a 3-ring configuration as shown in Figure 3.3. Each of the MARC sensors are labeled with a number from 1 to 20, and is how the MARC sensors will be referred to from this point on.

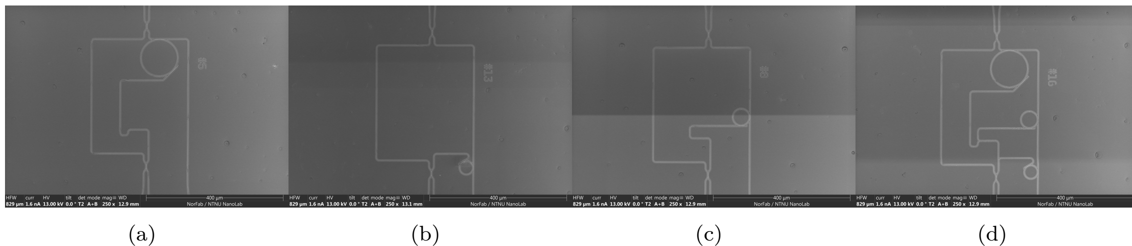

(a) (b) (c) (d)

Figure 5.13: SEM Overview of all four different configurations for the MARC sensor. Images are taken with SE signal, 13.0 kV, and 250x magnification. a) Fabricated MARC135 5, b) Fabricated MARC90 8, c) Fabricated MARC240 13, d) Fabricated multiplexed 3-ring MARC 16.

Some of the MARCs were imaged in the scanning electron microscope (SEM), and can be seen in Figure 5.13. This was to verify that the alignment worked properly, and that the designs was identical to the mask created.

Earlier in the project a cross-sectional image was taken of a dose test wafer. This was to ensure that the sidewall profile was close to straight, and that the etching process yielded a 220 nm thick a-Si layer. It also verified that the SiO_2 layer was 1

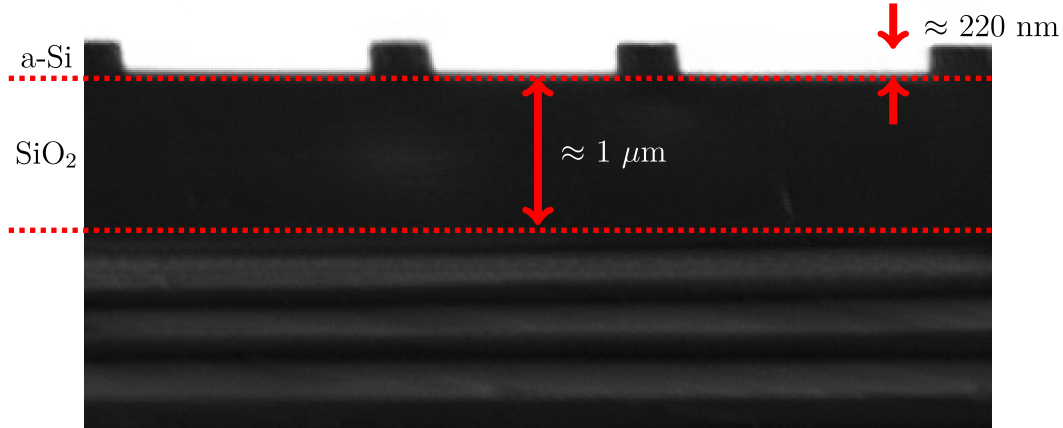

Figure 5.14: Cross-sectional SEM image of two waveguides. BSE signal, 3 kV, 20,000x magnification. The sidewalls on the left and right-hand sides are not waveguides, but the edges of the trenches.

μm, as promised by the manufacturer. The sample was scribed by hand, but resulted in a clean break. The cross-sectional image from the SEM can be seen in Figure 5.14.

5.2.6 MARC Measurements

The following sections will present the transmission spectrums from the fabricated MARC sensors. It is worth mentioning that the wafer chip was damaged in the final scribing step, as mentioned in Section 5.2.5. Coupling between the input/output and the fibers were achieved, but the transmission spectrum of the different MARCs did turn out to be quite noisy, i.e. transmission signal was beyond readable.

The laser operates over a wavelength interval from 1500 nm to 1580 nm. Although the laser did showcase wavelength dependencies, the measurements were carried out at the same interval as the MARC simulations.

5.2.7 MARC240

The transmission spectrum for the MARC240 is shown in Figure 5.15. The peaks observed at 1529 nm, 1537.5 nm, 1539 nm, and 1541.5 nm are very sharp. Compared to the peaks from the simulated MARC240 in Figure 5.8, the Q-factor is $\approx$ 16300.

Another observation is that the FSR is reduced to roughly 25% of the simulated MARC240's FSR. If we look at the refractive index of a-Si, which is wavelength dependent [52], it is clear that the assumption of a wavelength independent effective refractive index has been a simplification. As assumed in Equation 2.41, the effective

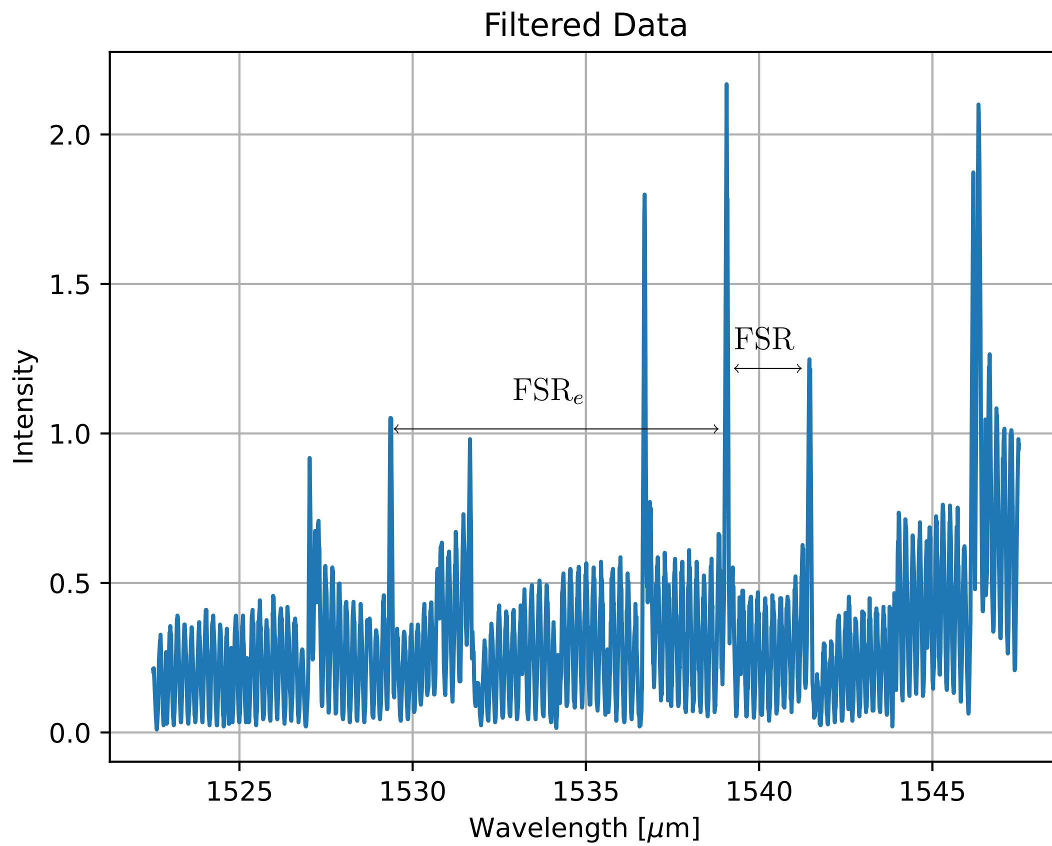

Figure 5.15: Transmission spectrum of the MARC240. The ripples are high and dense, but the signal is readable. The $FSR_e \approx 10.5$ nm and $FSR \approx 1.75$ nm.

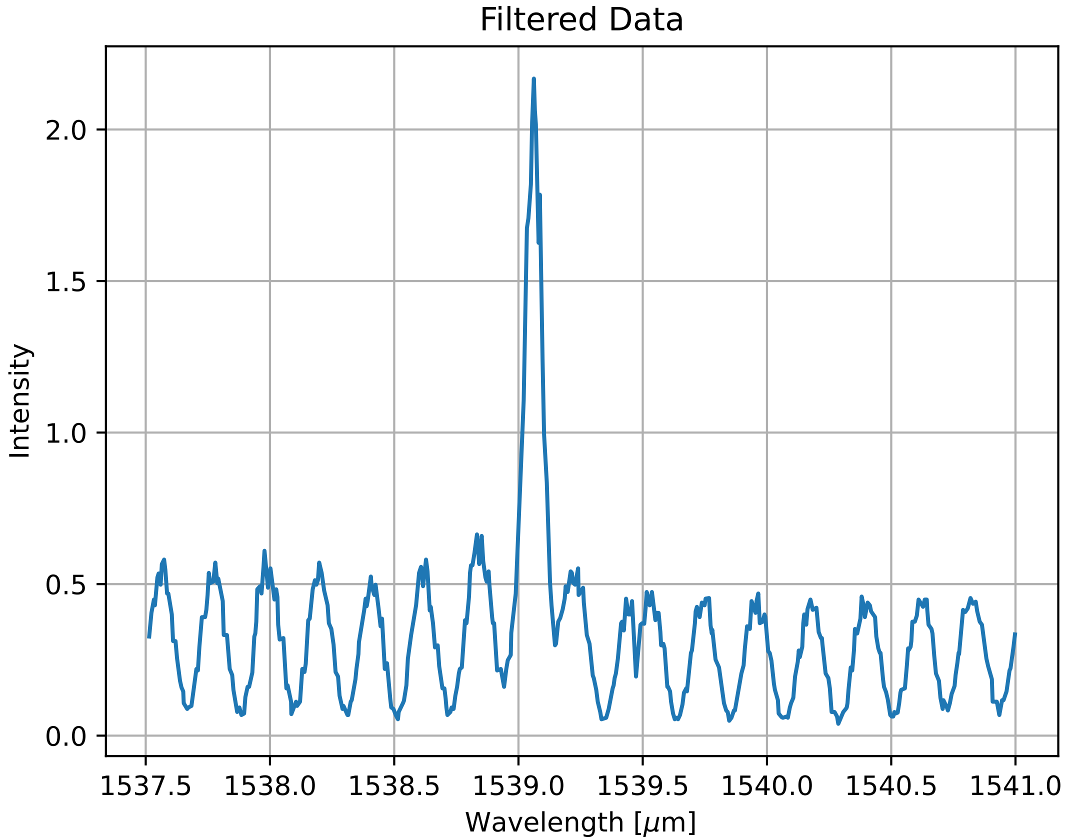

Figure 5.16: Transmission spectrum of the fabricated MARC240 sensor. The periodicity of the noisy ripples reassembles a Fabry-Perot resonator.

refractive index n_{eff} is dispersionless. This could be one of the reasons for the big difference in FSR between the simulated and fabricated MARC240.

As mentioned several times throughout this project, the Fabry-Perot ripples are present in the simulations. The repeated ripples that seems to correspond to a Fabry-Perot resonator. In Figure 5.16, which is of the fabricated MARC240, the ripples seems to correspond to a Fabry-Perot resonator.

5.2.8 MARC90

The transmission spectrum of the MARC90 can be seen in Figure 5.17. Compared to the transmission spectrum of the MARC240, this signal does not resemble the simulated transmission spectrum. This is most likely due to the output signal being scattered, and thus not being able to couple into the fiber.

The seeming asymmetrical signal from the fabricated MARC90 does not show the same Fabry-Perot periodicity and uniformity as the fabricated MARC240 sensor.

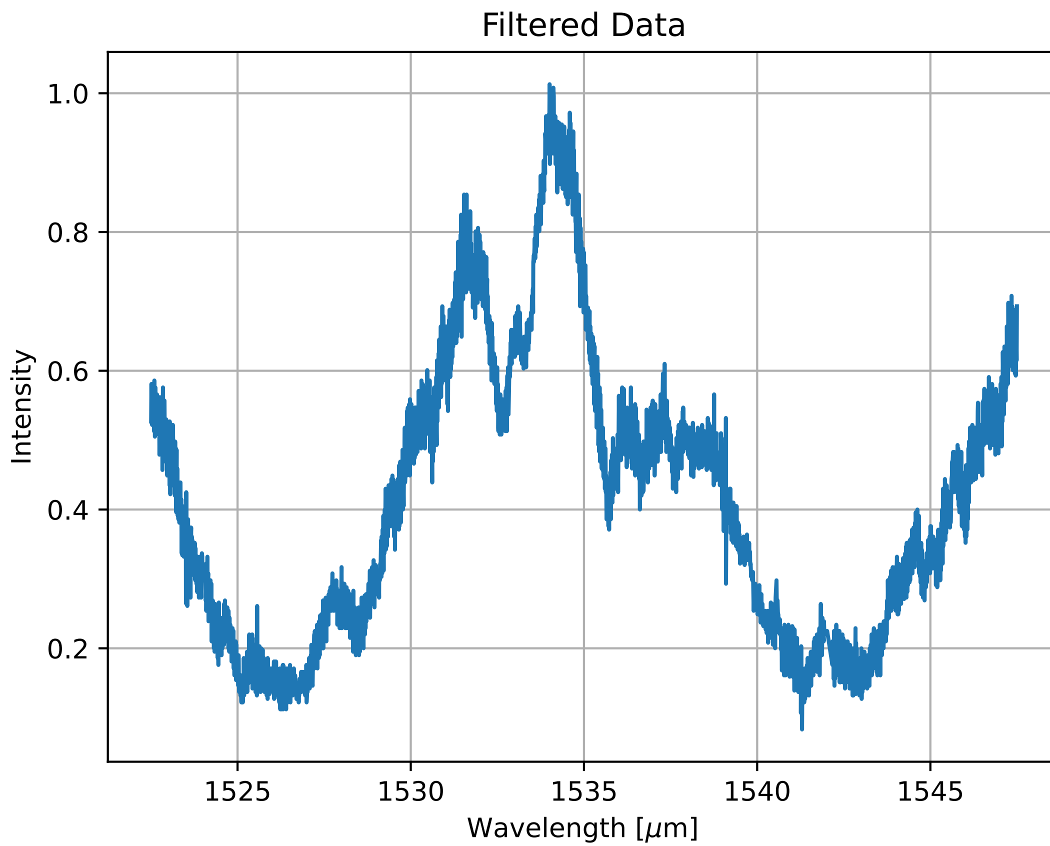

Figure 5.17: Transmission spectrum of the MARC90. The signal is unreadable and influenced by high noise. The FSR_e and FSR can not be determined.

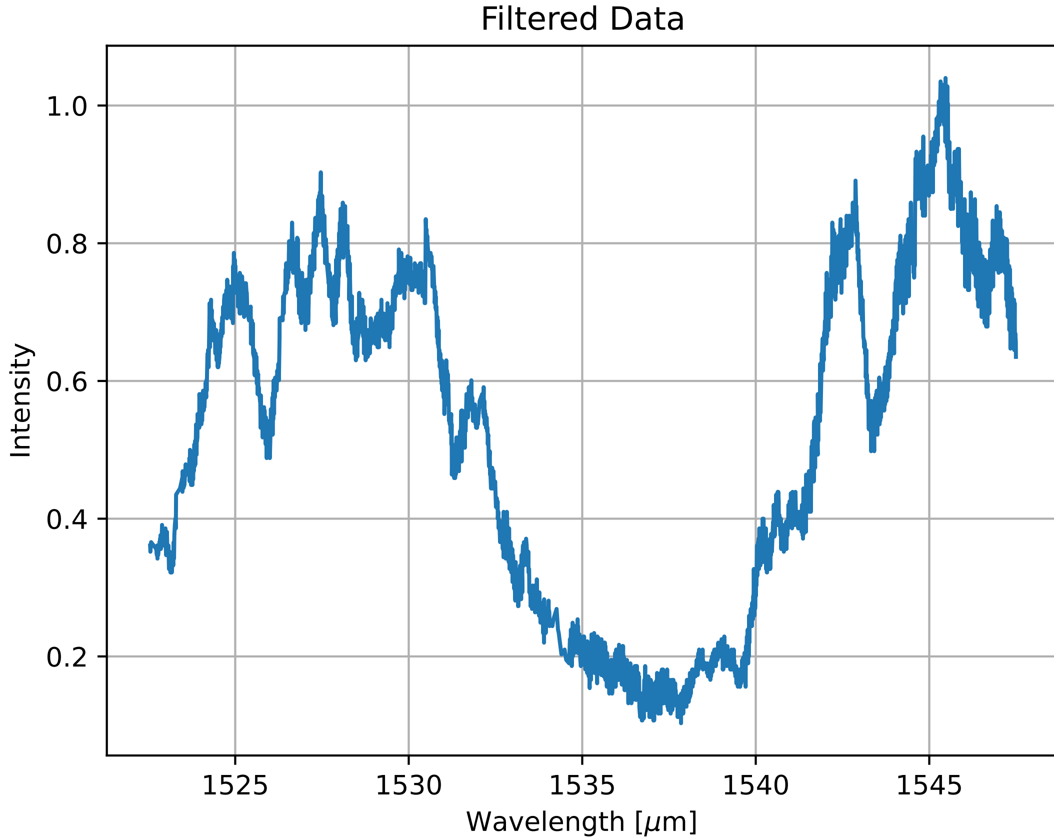

Figure 5.18: Transmission spectrum of the MARC135. There are high noise throughout the entire spectrum. It is not possible to determine FSR_e and FSR when the noise is too high.

This could be overshadowed by the noise in the laser and detector. If we compare the intensity of the fabricated MARC240 and fabricated MARC90, the intensity is at it's highest ≈ 1 [a.u]. Between 1540 nm and 1545 nm, the signal does not exceed an intensity of ≈ 0.4 [a.u].

This is most likely a fabrication fault, and could be the result of improper scribing as explained in Section 5.2.5. To avoid this, the wafer chip should be scribed only at the edges oppose to scribing over the entire waveguide structure.

5.2.9 MARC135

The transmission spectrum of the fabricated MARC135 can be seen in Figure 5.18. This signal is very similar to the signal from the fabricated MARC90. Both signals have a dip in intensity, and are not close to reach the intensity of the fabricated MARC240.

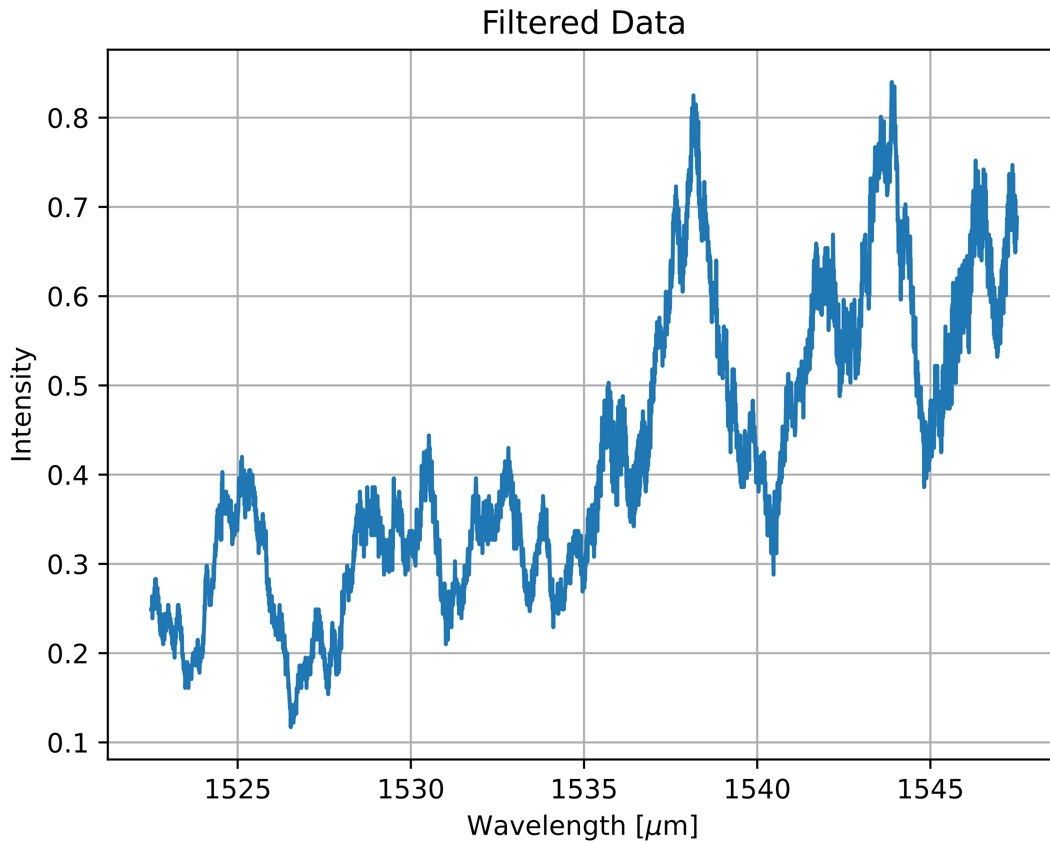

Figure 5.19: Transmission spectrum of the Multiplexed MARC sensor. There are several "peaks", where the intensity reaches a maximum. However, these maximums are not characterized as resonant peaks.

5.3 Multiplexed MARC

The transmission spectrum of the Multiplexed MARC can be seen in Figure 5.19. Similar to the transmission spectrum of the MARC90 and MARC 135, there signal does not give any useful information. Here the signal does not show any observable lineshapes, such as the Fano lineshape and Lorentzian lineshape.

6 Conclusion

6.0.1 Simulations

Three different MARC devices were created in COMSOL using the finite-elements method. All were created in the same geometry, making it possible to multiplex the devices in the future. When MARC240, MARC90, and MARC135 were simulated independently, they yielded a transmission response which could be analyzed.

The transmission signal was readable, although varying for the three different devices. The fact that the FSR_e is around 5 folds the value of FSR, the MARC devices shows promising results towards the fabrication process in the future.

Further balancing of individual MARC devices, a multiplexed signal can be realised. When the discrepancies are accounted for, such as the coupling in the 3dB coupler, absorption losses in the waveguide bends, and phase imbalances in the interferometer arms, the device can be fabricated in a lab.

6.0.2 Fabrication

The fabricated MARC sensors did show potential, especially with the MARC240. This was likely due to a clean break when scribing, while the other output ports along the wafer chip was damaged. However, the process of realizing the MARC sensor seems to be optimized. The detailed step-by-step process described in Section 4.2 has been tried out and completed several times. At the end the wafer chip was clean and showing good etch profiles. Also the inverted tapers did eventually survive the process, without being damaged during one of the steps in Section 4.2.4. The main focus of this project has been the fabrication, as it had to be optimized before being able to measure a MARC sensor. Therefore, during this project only a single wafer chip was measured.

It turned out that it was only the fabricated MARC240 that gave the desired lineshapes, but also this MARC sensor was influenced by high noise. The other MARC sensors, namely the MARC90, the MARC135 and the multiplexed MARC showed high noise. These sensors were likely not able to couple properly, due to the scattering at the output.

7 | Further Work

There are several portions of this project that needs to be improved upon. Firstly the COMSOL simulations are not perfect, and the geometry still needs to be balanced properly. Namely the MARC135 was a problem during this project, and the next step might be to redesign the optical path of the MARC135.

The fabrication process does yield a lot of the desired parameters, i.e. 220 nm thick a-Si, straight etch profile, 2 μm thick SU-8 resist layer. However, there is no doubt that the chip suffered from an imperfect fabrication process.

Unfortunately towards the end of the project, when I was ready to make several identical wafer chips, the EBL was down for maintenance. This meant that there was only one chip that could be measured, which was far from ideal. In the future, the creation of several wafer chips will not only result in a better fabrication routine, but will also reduce the chance of damaging the waveguide structure in what should be simple process steps.

Another vital part of the fabrication of the MARC sensors, is to actually make sure that each of the individual ring resonators are created with critical coupling. This was not done in this project, and the coupling distance was based solely upon the simulated results. This is something that should be done if this projected is to be continued upon.

References

[1] Moe, S. (2022). “Simulation of Mach-Zehnder Interferometer-Assisted Ring Resonator Configuration (MARC) Photonic Sensors”. Project Thesis. Norwegian Univeristy of Science and technology.

[2] Yadav, M. et al. (2021). “Spectral shaping of ring resonator transmission response”. *Optics Express* 29 (3) 3764.

[3] Yadav, M. and Aksnes, A. (2022). “Multiplexed Mach-Zehnder interferometer assisted ring resonator sensor”. *Optics Express* 30 (2) 1388.

[4] Riley, J. C. (2005). “Estimates of Regional and Global Life Expectancy, 1800-2001”. *Population and Development Review* 31 (3) 537–543.

[5] Amano, Y. and Cheng, Q. (2004). “Detection of influenza virus: traditional approaches and development of biosensors”. *Analytical and Bioanalytical Chemistry* 381 (1) 156–164.

[6] Manabe, Y. C., Sharfstein, J. S., and Armstrong, K. (2020). “The Need for More and Better Testing for COVID-19”. *JAMA* 324 (21) 2153.

[7] Steglich, P. et al. (2019). “Optical Biosensors Based on Silicon-On-Insulator Ring Resonators: A Review”. *Molecules* 24 (3) 519.

[8] Prasad, P. (2003). *Introduction to Biophotonics*. Wiley-Interscience publication. Wiley.

[9] Yamada, K. et al. (2014). “High-performance silicon photonics technology for telecommunications applications”. *Science and Technology of Advanced Materials* 15 (2) 024603.

[10] Bogaerts, W. et al. (2004). “Basic structures for photonic integrated circuits in Silicon-on-insulator”. *Optics Express* 12 (8) 1583.

[11] Estevez, M., Alvarez, M., and Lechuga, L. (2011). “Integrated optical devices for lab-on-a-chip biosensing applications”. *Laser & Photonics Reviews* 6 (4) 463–487.

[12] Saleh, B. E. A. and Teich, M. C. (2019). *Fundamentals of photonics; 3rd ed.* Wiley series in pure and applied optics. New York, NY: Wiley.

[13] Cheng, D. (1989). *Field and Wave Electromagnetics*. Addison-Wesley series in electrical engineering. Addison-Wesley.

[14] Born, M. and Wolf, E. (2019). *Principles of Optics*. Cambridge University Press.

[15] Reed, G. T. and Knights, A. P. (2004). *Silicon Photonics*. Wiley.
[16] Feng, S. et al. (2011). "Silicon photonics: from a microresonator perspective". *Laser & Photonics Reviews* 6 (2) 145–177.
[17] Rabus, D. and Sada, C. (2020). *Integrated Ring Resonators: A Compendium*. Springer Series in Optical Sciences. Springer International Publishing.
[18] Chiang, K. S. (1991). "Performance of the effective-index method for the analysis of dielectric waveguides". *Optics Letters* 16 (10) 714.
[19] *Silicon-On-Insulator (SOI) Technology* (2014). Elsevier.
[20] Sparacin, D., Spector, S., and Kimerling, L. (2005). "Silicon waveguide sidewall smoothing by wet chemical oxidation". *Journal of Lightwave Technology* 23 (8) 2455–2461.
[21] Selvaraja, S. K. et al. (2009). "Fabrication of Photonic Wire and Crystal Circuits in Silicon-on-Insulator Using 193-nm Optical Lithography". *Journal of Lightwave Technology* 27 (18) 4076–4083.
[22] *Materials Science of Thin Films* (2002). Elsevier.
[23] Quirk, M. and Serda, J. (2001). *Semiconductor manufacturing technology*. Vol. 1. Prentice Hall Upper Saddle River, NJ.
[24] Ohring, M. (1992). "The materials science of thin films". *Appl. Opt* 31 (34) 7162.
[25] Stepanova, M. and S. Dew, eds. (2012). *Nanofabrication*. Springer Vienna.
[26] Egerton, R. F. et al. (2005a). *Physical principles of electron microscopy*. Vol. 56. Springer.
[27] Shawn, C., Makiuchi, Y., and Che, C. (2010). "High-energy Electron Beam Lithography for Nanoscale Fabrication". *Lithography*. InTech.
[28] Karouta, F. (2014). "A practical approach to reactive ion etching". *Journal of Physics D: Applied Physics* 47 (23) 233501.
[29] Legtenberg, R. et al. (1995). "Anisotropic Reactive Ion Etching of Silicon Using SF 6 / O 2 / CHF 3 Gas Mixtures". *Journal of The Electrochemical Society* 142 (6) 2020–2028.
[30] Mogab, C. J. (1977). "The Loading Effect in Plasma Etching". *Journal of The Electrochemical Society* 124 (8) 1262–1268.
[31] Tang, Y.-H. et al. (2015). "Investigation of fabricated Through Glass Via (TGV) process by inductively coupled plasma reactive ion etching of quartz glass". *10th IEEE International Conference on Nano/Micro Engineered and Molecular Systems* 401–404.
[32] Roxhed, N., Griss, P., and Stemme, G. (2007). "Tapered Deep Reactive Ion Etching: Method and Characterization". *TRANSDUCERS 2007 - 2007 International Solid-State Sensors, Actuators and Microsystems Conference* 493–496.
[33] Bogalecki, A. and Plessis, M. du (2010). "Design and Manufacture of Quantum-Confined SI Light Sources". *SAIEE Africa Research Journal* 101 (1) 11–16.

[34] Cao, G. and Wang, Y. (2011). *Nanostructures and Nanomaterials*. WORLD SCIENTIFIC.

[35] Shawky, M. et al. (2016). "A Study on Synthesis and Characterization of Some (I -IV -VI) Groups Compounds for Solar Cells Energy Application For Partial Fulfillment of the Requirements for The Master Degree of science in Chemistry (Physical Chemistry) The Former CMRDI President". PhD thesis.

[36] Khursheed, A. (2011). *Scanning electron microscope optics and spectrometers*. World scientific.

[37] Egerton, R. F. et al. (2005b). *Physical principles of electron microscopy*. Vol. 56. Springer.

[38] Marturi, N. (2013). "Vision and visual servoing for nanomanipulation and nanocharacterization in scanning electron microscope."

[39] Palik, E. (1998). *Handbook of Optical Constants of Solids*. Academic Press handbook series v. 3. Elsevier Science.

[40] Holmgaard, T. et al. (2010). "Design and Characterization of Dielectric-Loaded Plasmonic Directional Couplers". *Lightwave Technology, Journal of* 27 5521–5528.

[41] Maszara, W. (1991). "Silicon-On-Insulator by wafer bonding: A review". *Journal of the Electrochemical Society* 138 (1) 341.

[42] Cacciatore, M. and Rutigliano, M. (2009). "Dynamics of plasma–surface processes: E–R and L–H atom recombination reactions". *Plasma Sources Science and Technology* 18 (2) 023002.

[43] Filmetrics (2006). *F20 - Taking the mystery out of the thin film measurements*.

[44] *SU-8 2000 Permanent Negative Epoxy Photoresist* (2015). d. MicroChem.

[45] Frieser, R. and Mogab, C. (1981). "Plasma Processing: Proceedings of the Symposium on Plasma Etching and Deposition". Electrochemical Society.

[46] *XP SU-8 Release Layer* (2019). Rev. 3. MicroChem.

[47] Pan, F. et al. (2008). "Improved Micro-Patterning of Soft-Polymers and Elastomers Using Conformally Coated Omni-Coat Nanofilms". *ASME International Mechanical Engineering Congress and Exposition*. Vol. 48746 281–286.

[48] Morino, H., Maruyama, T., and Iiyama, K. (2014). "Reduction of Wavelength Dependence of Coupling Characteristics Using Si Optical Waveguide Curved Directional Coupler". *Journal of Lightwave Technology* 32 (12) 2188–2192.

[49] Gupta, R. K., Chandran, S., and Das, B. K. (2017). "Wavelength-Independent Directional Couplers for Integrated Silicon Photonics". *Journal of Lightwave Technology* 35 (22) 4916–4923.

[50] Bogaerts, W. et al. (2012). "Silicon microring resonators". *Laser & Photonics Reviews* 6 (1) 47–73.

[51] Xiao, Y.-F. et al. (2010). "High quality factor, small mode volume, ring-type plasmonic microresonator on a silver chip". *Journal of Physics B: Atomic, Molecular and Optical Physics* 43 (3) 035402.

[52] Pierce, D. T. and Spicer, W. E. (1972). “Electronic Structure of Amorphous Si from Photoemission and Optical Studies”. *Physical Review B* 5 (8) 3017–3029.